Journal of Materials Chemistry A

Accepted Manuscript

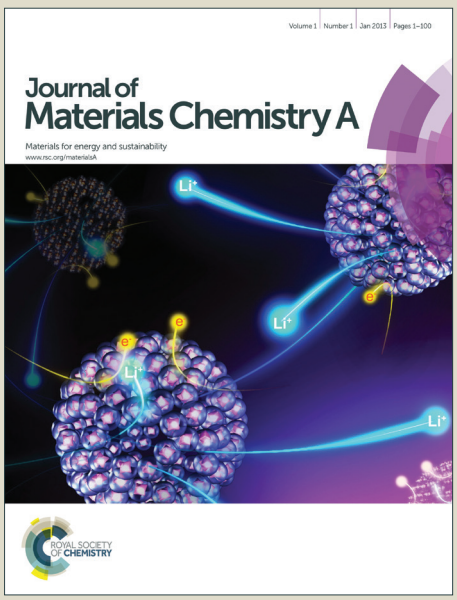

ROYAL SOCIETY OF CHEMISTRY

www.rsc.org/materialsA

Array Geometry Dictates Electrochemical Performance of Ge Nanowire Lithium Ion Battery Anodes

Behdokht Farbod [a,b*], *Kai Cui* [b], *Martin Kupsta* [b], *W. Peter Kalisvaart* [a,b], *Elmira Memarzadeh* [a,b], *Alireza Kohandehghan* [a,b] *Beniamin Zahiri* [a,b], *David Mitlin*[a, b*]

[a]: University of Alberta Department of Chemical and Materials Engineering, 9107 116th Street, T6G 2V4, Edmonton, AB, Canada.

[b]: National Institute for Nanotechnology (NINT), NRC, 11421 Saskatchewan Dr., Edmonton, AB, T6G 2M9, Canada

* behdokht@ualberta.ca, *dmitlin@ualberta.ca

Abstract

Scientific literature shows a substantial study-to-study variation in the electrochemical lithiation performance of "1-D" nanomaterials such as Si and Ge nanowires or nanotubes. In this study we varied the vapor-liquid-solid (VLS) growth temperature and time, resulting in nanowire arrays with distinct mass loadings, mean diameters and lengths, and thicknesses of the parasitic Ge films that are formed at the base of the array during growth. When all the results were compared, a key empirical trend to emerge was that increasing active material mass loading

drastically degraded the electrochemical performance. For instance, GeNWs grown for 2 minutes at 320 °C (0.12 mg cm^{-2} mass loading, 34 nm mean nanowire diameter, 170 nm parasitic film thickness) had a reversible capacity of 1405 mAh g^{-1}, a cycle 50 coulombic efficiency (CE) of 99.9%, a cycle 100 capacity retention of 98%, and delivered ~ 1200 mAh g^{-1} at 5C. To contrast, electrodes grown for 10 minutes at 360°C (0.86 mg cm^{-2}, 115 nm, 1410 nm) retained merely 5.6% of their initial capacity after 100 cycles, had a CE of 96%, and delivered ~ 400 mAh g^{-1} at 5C. Using TOF-SIMS we are the first to demonstrate marked segregation of Li to the current collector interface in planar Ge films that are 300 and 500 nm thick, but not in the 150 nm specimens. FIB analysis shows that the cycled higher mass loaded electrodes develop more SEI and interfacial cracks near the current collector. A comparison with the state-of-the-art scientific literature for a range of Ge - based nanostructures shows that our low mass loaded GeNWs are highly favorable in terms of the reversible capacity at cycle 1 and cycle 100, steady-state cycling CE and high-rate capability.

Keywords: Ge, nanowire, thin film, Li segregation, SEI, TEM, FIB, TOF-SIMS

Introduction

Lithium ion batteries (LIBs) are rechargeable batteries meeting high power density demands of the portable electronic and implantable devices as well as electric and hybrid electric vehicle. [1-3] Commercial LIB anodes are primarily based on graphite, in which a maximum theoretical specific capacity of 372 mAh g^{-1} may be achieved. [4] Since this capacity is less than that required for high-energy applications, alternative anode materials are being sought.

Germanium with the theoretical capacity of 1624 mAh g^{-1} ($Li_{22}Ge_5$) is considered to be a promising alternative [5-7]. Despite its higher price, Ge has some advantages over Si, including 10^4 times higher electrical conductivity, and 400 times higher lithium diffusivity at room temperature. [8-10] Compared to Si, Ge forms a much less tenacious native oxide at its outermost layer, resulting in a decreased Li_2O formation during first lithiation and thereby an improved initial coulombic efficiency. [11] However, similarly to Si, the high internal strains in Li-active Ge lead to structural disintegration, pulverization, loss of electronic contact, and ultimately poor capacity retention. [12-14] While attractive in terms of energy density, Ge also suffers from a very large volume expansion/shrinkage during lithium insertion/extraction. As a comparison, graphite expands 10% upon lithiation to LiC_6, [15] $Li_{22}Ge_5$ exhibits 370 % [5] volume expansion.

To improve capacity retention many strategies have been recently implemented using Ge planar films, [11,16-21] nanoparticles, [10,22-30] nanotubes, [31] alloyed nanocrystals, [32,33] and "1-D" nanowires. [8,34-43] Such structures are also expected to demonstrate improved rate capability due to the high specific surface area available for Li uptake and charge transfer. [44] However, the large surface area is also a disadvantage, leading to formation of copious amounts of solid electrolyte interphase (SEI) and an accompanying irreversible capacity loss. [45-49] Being manufacturable en-masse through various VLS and solution growth mechanisms, Ge nanowires (GeNWs) remain highly scientifically interesting. Lithiation and expansion of Ge nanowires has been reported to proceed isotropically, [50-52] contrary to the dumbbell-shapes that develop in SiNWs. [49,53,54] Early studies on GeNWs reveal that the cycling stability requires further improvement [35-42] and that it varies substantially from study to study. For instance, authors in [38] reported a capacity loss of 65.7% for bare GeNWs, cycled 50 times at the rate of 0.1C. Losses higher than 50% over the

first 20 cycles have been reported as well. [39] Other studies show that GeNWs grown directly on a current collector are generally more favorable. [39-41,55] VLS-grown GeNWs using chemical vapor deposition (CVD) from GeH_4 showed ~1000 mAh g^{-1} capacity at 0.05C over the first 20 cycles [40]. Failure modes for GeNWs appear to be distinct form their Si counterparts. For instance highly anisotropic expansion followed by break-up into thinner filaments has been observed during lithiation of SiNWs. [52,53,56,57] GeNWs, on the other hand, expands more isotropically becoming porous over the course of cycling. [58]

Our original objective was to investigate the role of GeNW array geometry on its cycling capacity retention and rate capability as a lithium ion battery anode. Remarkably, despite a large number of high quality studies (e.g. those cited in this Introduction and in Table 3) on a given GeNW array with a fixed architecture, the actual role of the mean nanowire length, diameter, etc. on the electrochemical performance has not been explicitly examined. While there is some (primarily modeling) work on geometric-aspects of the lithiation behavior of Si nanowires, as will be discussed in the main manuscript, the two systems are sufficiently distinct. The mean nanowire diameters and lengths in the arrays were tuned by changing the vapor-liquid-solid (VLS) growth temperatures (320°C and 360°C) and times (2, 5 and 10 minutes). We started with a hypothesis that thicker nanowires will fail at faster rates due to the higher differential stresses incurred between their lithiated and non-lithiated sections. For a given growth temperature, this relationship was indeed observed. We also documented a factor of 3X improvement in the electrodes' rate capability when the mean nanowire diameter was halved. When the capacity retention and steady-state coulombic efficiency were plotted against the electrode mass loading, there was a clear empirical tend of decreasing performance with higher loading that spanned an

order of magnitude in active material weight (~ 0.1 - 1 mg cm^{-2}). Such a strong correlation has never been reported in literature for either Ge or Si nanowires. This study is also the first to examine the role of the parasitic thin film layer sitting at the base of the nanowire arrays in establishing the cycling performance of Ge nanowires. Parasitic films are widely reported in literature for VLS grown Si and Ge nanowires [59-65] and have been recently examined by Picraux et al. [59] only for the case of Si. However their role remains unexplored for the fundamentally different case of Ge nanowires. Time of Flight Secondary Ion Spectroscopy (TOF-SIMS) is a powerful emerging technique that is becoming employed to analyze Li interfacial segregation in Si and Sn [66,67,68,69] and Na segregation in Sn alloy films. [70] Here we are the first to employ TOF-SIMS to probe Li segregation in Ge, delivering a finding that such segregation does indeed occur but is highly thickness dependent, with consequently profound implications on the mechanical performance of a range of Ge-based electrodes. Finally we provide a systematic comparison of the performance of our best GeNW arrays with a range of state-of-the-art Ge nanostructures reported in literature. We demonstrate that our materials are among the best in terms of a range of key parameters, such as the initial capacity, the cycling capacity retention, the cycling coulombic efficiency and the rate capability.

Experimental Procedure

Germanium nanowires (GeNWs) of varying mass loadings were grown on commercial 316 stainless steel spacers (MTI Corporation) that were polished down to 0.05 micron. The nanowires were grown in a commercial CVD tube furnace (Tystar, Inc.) by the vapor-liquid-solid (VLS) mechanism. A 200 nm TiN conductive diffusion barrier layer and a 10 nm Au seed catalyst layer were employed. The furnace was heated up to the growth temperature, either 320

or 360 °C, at 10 ºCmin^{-1} under a flow of Ar and H_2. Even though 320 ^{o}C is well below the eutectic temperature of Au-Ge, nanowire growth can still occur by the VLS mechanism. When the Au catalyst particles are in the order of several tens of nanometers, the eutectic point can shift to lower temperature. [60,71] To dewet the Au catalytic film, the substrates were held at the growth temperature for 1 hour prior to introducing GeH_4. During the growth process, a mixture of GeH_4:H_2 with a flow ratio of 1:4 was used as a working gas and the total pressure of chamber was set at 100 Torr. Three different growth times, 2, 5, and 10 minutes, were employed.

Standard 2032 half-cells were assembled using lithium metal foil as the counter electrode and polyethylene separators (MTI Corporation, porosity of 36-44% and average 0.03 μm pore size). The spacers were weighted before and after GeNWs deposition. The microbalance employed (Mettler Toledo, XP6U) had a manufacturer quoted 0.1 μg accuracy. 1 M lithium hexafluorophosphate ($LiPF_6$) salt in 1:1:1 volume ratio of ethylene carbonate:dimethyl carbonate: diethyl carbonate (EC:DMC:DEC) was used as electrolyte. The assembly process was carried out in an argon-filled glovebox in which oxygen and moisture concentration levels were kept below 0.2 ppm. Galvanostatic charge-discharge measurements were carried out on a BT2000 Arbin potentiostat at a potential range of 0.01-2 V vs. Li/Li^+ and a constant current (CC) density. Cyclic voltammetry (CV) experiments were carried out using a Solartron 1470 Multistat system with Corrware data acquisition software, in which the potential was scanned in a range of 0.01-2 V vs. Li/Li^+ with a scan rate of 1 mV s^{-1} for 10 cycles. After testing, the samples were disassembled in order to do post-cycling characterization of the microstructure. The cycled electrodes were soaked and rinsed in acetonitrile and kept overnight in the glovebox to remove residual electrolyte. All testing was performed at room temperature.

The as-grown and cycled nanowire samples were characterized using scanning electron microscopy (SEM) (Hitachi FESEM S-4800) and transmission electron microscopy (TEM) (JEOL 2100, 200 kV). Cross-sectional images of cycled electrodes were obtained using a dual beam FIB/SEM (Hitachi NB5000). Electron diffraction patterns were simulated using the commercial software Crystal Maker ™ and open-source software Diffraction Ring Profiler, [72] with the input of known space group information of Ge (Fd3m, 5.6578, 5.6578, 5.6578, Wyckoff position: 8a). Electron energy loss spectroscopy (EELS) measurements were conducted using scanning TEM (STEM) (JEOL 2200FS, 200 kV) with a nominal analytical beam size of 0.5 nm. High angle annular dark field (HAADF) images were also recorded simultaneously with the EELS analysis. We mapped Ge, C and O by integrating over core-loss edges of Ge-L, C-K, and O-K edge, respectively. Lithium maps for cycled materials were obtained from the low-loss Li-K edge at 60-70 eV. Digital Micrograph (Gatan, Inc.) was employed for signal collection and data extraction from EELS spectra. XPS measurements were conducted on an ULTRA (Kratos Analytical) spectrometer under ultrahigh vacuum (10^{-9} Torr), using monochromatic Al-K_α radiation (hv = 1486.6 eV) operated at 210 W. The high-resolution spectra were collected with an energy window of 20 eV. The XPS data were analyzed using CasaXPS software. Planar Ge thin films were depth analyzed using time-of-flight secondary ion mass spectroscopy (TOF-SIMS) instrument, ION-TOF GmbH. The analysis chamber was kept at a pressure of $< 5 \times 10^{-9}$ mbar. 1 kV O_2 ions with current of ~ 40 nA were used for sputtering over an area of 200 × 200 μm^2 and a 25 kV Bi ion source was used for analysis over an area of 40 × 40 μm^2.

Results and Discussion

The GeNWs were grown for three different growth times, 2, 5, and 10 minutes, at temperatures of 320°C or 360°C. For the remainder of manuscript, the samples will be labeled according to their mass loading which corresponds to a specific growth temperature - time combination: 0.12mg-(320/2min), 0.31mg-(320/5min), 0.73mg-(320/10min), 0.2mg-(360/2min), 0.52 mg-(360/5min), 0.86 mg-(360/10min).

Plan - view and cross-sectional images of as-grown nanowires for 0.12mg-(320/2min), 0.2mg-(360/2min), 0.52mg-(360/5min) are shown in Figure 1. The samples 0.31mg-(320/5min), 0.73mg-(320/10min) and 0.86mg-(360/10min) are shown in the supplemental, Figure S1. The wires are all shown at the same magnification. The high-magnification insets show that the 0.52mg-(360/5min) and 0.86mg-(360/10min) nanowires possess a two-tiered morphology. The top parts of the nanowires, below the Au catalyst droplets at the tips, are smooth, whereas further down the nanowire there is a transition to a different morphology where the surface becomes much rougher and tapered. The nanowire diameter and length distribution histograms are shown in Figure 2. Approximately 200 nanowires were analyzed per synthesis condition. With longer growth times not only does the mean nanowire diameter increase, but the overall diameter distribution broadens.

In addition to being present as crystalline nanowires, the Ge is also present as a largely continuous parasitic thin film layer sitting at the base of the array. The arrows in the cross-sectional images mark these films, with the associated numbers representing their mean thickness and standard deviation. It is important to point out that parasitic films are not a particularity of our CVD process (which was performed in a commercial nanowire growth

reactor), but are a fairly universal feature of Ge and Si nanowire growth through VLS. For instance, Cho and Picraux have recently detailed the ubiquity of parasitic layers (in that case semicontinuous islands) at the nanowire base for VLS Si nanowires. [59] The authors demonstrated that their formation could only be avoided by growth involving a tailored anodized aluminum oxide template. For the case of VLS Ge nanowires, parasitic islands near the current collector were reported in a range of studies. [60-65] In our samples, with increasing growth time and with a higher growth temperature the parasitic Ge layers thickened.

Table 1 provides the mean and standard deviation values for the nanowire length, the nanowire diameter and the parasitic layer thickness, for each synthesis conditions. For the more tapered nanowires grown at 360°C, the diameter was measured in the middle of the nanowire. For a given temperature, higher growth times also lead to longer nanowires. However, the nanowires grown at 360°C are consistently shorter than the ones grown for the same duration at 320°C. For a given growth duration the higher growth temperature also yields a higher Ge mass loading.

Figure S2 shows conventional and high resolution TEM analysis for the 0.12mg-(320/2min), 0.73mg-(320/10min) and 0.86mg-(360/10min) specimens. The 320°C grown nanowires are primarily single crystal or twinned single crystal. The 360°C grown nanowires are also single crystal at their core, but contain a substantial fraction of secondary Ge nanocrystallites nucleated near the nanowire base. This is what is responsible for the tapered morphology especially observed in the 0.86 mg-(360/10min) sample. Figure S3 shows the XPS results of the as-synthesized electrodes. The presence of a minor oxygen peak in addition to a

strong Ge signal indicates that the as-grown nanowires are covered by a layer of oxide that is quite thin, likely in the single nanometer or sub nanometer range.

Table 1: Mean and standard deviation values for the nanowire length, nanowire diameter, and the thin film layer thickness versus processing conditions

Electrode	Mean diameter (nm)	Mean length (μm)	Mean thickness of Ge thin film (nm)
0.12mg-(320/2min)	34 ± 19	2 ± 0.7	170 ± 70
0.31mg-(320/5min)	35 ± 30	13 ± 3.5	310 ± 90
0.73mg-(320/10min)	106 ± 81	36 ± 8.3	860 ± 130
0.2mg-(360/2min)	64 ± 42	2 ± 0.7	220 ± 80
0.52mg-(360/5min)	88 ± 61	4 ± 1.5	790 ± 160
0.86mg-(360/10min)	115 ± 76	7 ± 2.0	1410 ± 280

In the VLS mechanism, the reactants are introduced via the decomposition of GeH_4 gas and dissolve into the catalyst to form a molten gold-germanium alloy. Super-saturation of the molten droplet by Ge finally leads to the nucleation and axial growth of the nanowires. [73,74] The presence of liquid phase in the VLS growth mechanism requires the NWs growth to be carried out at temperatures above the eutectic melting point of the Au-Ge binary system (360 °C). [63] However, the eutectic temperature may shift to lower values in nanoscale binary systems due to the capillary effects, making it possible to grow Ge nanowires at temperatures below 360 °C. [60,64,75,76] Germanium nanowires grown at temperatures near the bulk eutectic are reportedly tapered with thicker root and thinner top. [60,74,76,77] Tapering growth of nanowires can occur via two possible mechanisms. One mechanism, first reported by Hannon et al., [78] is due to the Au catalyst mass loss during the VLS process at high temperatures. Catalyst migration through the

surface of the nanowires will gradually consume the Au-containing alloy from the tip and make the droplet size smaller. This phenomenon induces further tapering growth of nanowires with non-uniform diameters. [76] Previous works on GeNWs [75,79] have shown that lowering the growth temperature can significantly decrease the surface diffusion of gold and the tapered growth of the NWs. Another mechanism can be the vapour-solid (VS) growth of the nanowires during the VLS process, probably due to the direct deposition of Ge on their sidewalls. [71,64] At high temperatures, the decomposition of GeH_4 can take place without the presence of the Au nanoparticles, leading to the deposition of Ge nanoparticles. [64] The lower sections of the NWs are exposed to a Ge source for longer time, leading to increased radial growth at these parts and thus tapering and irregular morphology. Since the nanowires become amorphous in their delithiated state after the first lithiation, it is their geometrical (i.e. diameter, length) rather than their crystallographic features that are important for electrochemical performance.

Figure 3 shows the cyclic voltammetry (CV) curves for all the materials. The order of presentation is (a) 0.12mg-(320/2min), (b) 0.31mg-(320/5min), (c) 0.73mg-(320/10min), (d) 0.2mg-(360/2min), (e) 0.52mg-(360/5min), (f) 0.86mg-(360/10min). The peak currents increase with increasing temperature/growth time, consistent with increasing mass loading per unit area. While the absolute current varies due to the different mass loading for each growth condition, qualitative shape of the CV's is analogous for each specimen. In the first cycle, crystalline Ge is transformed into a series of Li_xGe_y alloys. Over the course of cycling, there are three highly broadened reduction peaks centered near 0.45, 0.3 and 0.1 V, and a sharp oxidation peak near 0.7 V vs. Li/Li^+. In the CV of the 0.12mg-(320/2min) specimen these peaks are highlighted by arrows. The reduction peak near 0.1 V has been associated with the crystallization to $Li_{15}Ge_4$,

[80,81] with the reverse dissolution process having an oxidation peak too broad to detect separately. The remaining peaks may be attributed to compositional and structural (i.e. nearest neighbor arrangement) changes within the lithiating/delithiating Li_xGe_y. The associated phases would not be present on the equilibrium phase diagram and are yet to be well characterized. Similarly to the Li-Si system, the nucleation barrier for the intermediate Li-Ge phases of equilibrium crystal structure is expected to be too high at ambient temperature. It is reasonable to argue that these intermediate Li-Ge phases should rather be amorphous, as they are known to be in Li-Si.

Figure 3 also shows the constant current (CC) voltage versus capacity curves for all the electrodes, in the order of (a) 0.12mg-(320/2min), (b) 0.31mg-(320/5min), (c) 0.73mg-(320/10min), (d) 0.2mg-(360/2min), (e) 0.52mg-(360/5min), (f) 0.86mg-(360/10min). Testing was performed at a current density of 138 mA g^{-1}. The CC curves are shown for cycles 1, 2, 10, 50 and 100. The potential versus capacity curves for all electrodes are quite similar both upon lithium insertion at first cycle and during subsequent cycling, with the mean positions of the sloping plateaus agreeing with the broadened peaks in the CV profiles. With increased cycling the plateau around 0.1 V decreases in capacity, indicating progressively less crystallization to $Li_{15}Ge_4$. The same has been observed for SiNWs [48,82,83] and may be related to the fact that during cycling, the nanowires disintegrate and the individual filaments are too small to accommodate a phase boundary.

The GeNWs specimens are amorphous in their delithiated state. This is demonstrated in Figure 4, which displays HRTEM micrographs and the corresponding Fast Fourier Transforms

(FFTs) of two representative nanowires in the 0.12mg-(320°C/2min) arrays after their first delithiation.

As shown in Table 2, the cycle 1 coulombic efficiency (CE) of the nanowires is effectively independent of the Ge nanowire and underlying Ge film dimensions, or of the mass loading. Figure S4 shows a plot of the first cycle charge and discharge capacities versus cycle number versus mass loading, tested at 138 mAh g^{-1}. This is in contrast to what is known for Si nanowires where cycle 1 CE substantially depends on the nanowire dimensions and size distribution, e.g. being in the range of 94 - 83% depending on the geometry. [82] Moreover, the cycle 1 CE values (94.8 - 96.8) are in the range, albeit on the upper end, of what has been previously reported for a variety of Ge - based nanostructures. This is illustrated in Table 3, where the literature reported cycle 1 CE values run as high as 98.6% down to the low 30's. Interestingly the same wide variation is reported in scientific literature for graphite-based LIB anodes, with cycle 1 CE values ranging anywhere from 100% (within measurement accuracy) to 74.5%. Table S1 shows a comparison of the initial CE for literature published graphite and related materials - based LIB anodes. The associated references are provided in the supplemental.

For Si nanowires extensive modeling and experimental analysis shows that there is a critical diameter (200 - 300 nm range) above which the initially single or twinned single crystal nanowires are not able to withstand the initial lithiation stress and fracture catastrophically. [52,53,54,82,84-90] Full fracture during the first cycle then leads to immediate mechanical separation from the current collector. Any Li already present in the fractured wires is then not recovered,

leading to a lowering of the CE. Thicker crystalline blanket films of Si are similarly less able to withstand the anisotropic initial lithiation stress associated with the ~ 300% volume expansion. [84,91-95] However it has been recently demonstrated that 300 nm scale and even micro scale Ge particles behave fundamentally differently, not fracturing upon the initial lithiation. [96] This was explained in terms of the crystallographic isotropy of the lithiation process, with the stress state in Ge being much more uniform than in Si. Our cycle 1 results support this conclusion. Moreover comparing the cycle 1 capacity loss for the Ge nanowires in this study to the cycle 1 capacity loss for Si nanowires, shows that the roughly 4 - 7 % cycle 1 capacity loss for all the conditions tested here is on par with the CE loss in the most optimized Si nanowire arrays, i.e. the ones that have diameters largely below the critical fracture dimension. [48,82,83,97,98] The electrodes with larger Si nanowire dimensions lose as much as 17% capacity at cycle 1.

Figure 5(a) shows a plot of the reversible capacity (measured at delithiation) of all the specimens as a function of cycle number, going up to 100 cycles. The results are plotted in the order of increasing mass loading, which clearly highlights the key trend in performance. The capacity of the highest mass loaded specimen, 0.86mg-(360/10min), decays to 5.6% of the initial capacity by cycle 100. The second highest mass loading specimen, 0.73mg-(320/10min), retains 50% of its initial capacity at cycle 100. With lower mass loadings, the capacity progressively improves until it reaches 98% of its initial value for 0.12mg-(320/2min). According to Figure 5(b) the cycling coulombic efficiency of the electrodes also decreases on the order of higher mass loading. As Table 2 indicates, the CE values at cycle 100 range from nearly 100% (99.8%) for the 0.12mg-(320/2min) specimen to 88.1% for 0.86mg-(360/10min). As demonstrated in Figure 5(c), the 320°C and the 360°C synthesis temperature cycling capacity retention and CE

results converge into a fairly narrow single band of data when plotted against the Ge mass loading. Figure 5(d) shows a rate capability comparison between 0.12mg-(320/2min) and 0.2mg-(360/2min). The drastic difference in the rate capability is likely a result of the longer Li diffusion distances associated with the larger diameters of the nanowires and the thicker Ge films in the 0.2mg-(360/2min) electrodes, as shown in Table 1. At high rates there is insufficient time to lithiate through the thickness and only a fraction of the theoretical capacity is achieved.

Table 2: The reversible capacity and coulombic efficiency of GeNWs after the 1st and 100th cycle, tested at 138 mA g^{-1}

Electrode	**Capacity (mAh g^{-1})**		**Capacity retention (%)**	**Coulombic efficiency (%)**	
	1st	**100th**	**100th**	**1st**	**100th**
0.12mg-(320/2min)	1438	1408	97.9	94.8	99.8
0.31mg-(320/5min)	1426	1300	91.1	95.0	96.9
0.73mg-(320/10min)	1398	691	49.4	96.1	98.1
0.2mg-(360/2min)	1429	1262	88.3	93.3	96.7
0.52mg-(360/5min)	1331	1120	84.1	96.7	96.3
0.86mg-(360/10min)	1338	75	5.6	96.8	88.1

The role of electrode nanowire and parasitic film geometry on the cycling performance is highlighted in Figures 6. Figures 6(a) and 6(b) show the cycling capacity retention as a function of the mean nanowire diameter and of the Ge film thickness. These results highlight the strongest trends in performance. In both cases, there is a sharp monotonic decrease in the cycle 100 capacity with thicker nanowires and with thicker parasitic films. The role of nanowire (or nanoparticle) diameter and film thickness in establishing cycling electrochemical performance

has been treated extensively in scientific literature for the case of Si. [77,85] The general findings may be qualitatively applied for the case of Ge, which has received less attention to date, e.g. [17,18,52,99]. Both experimental and theoretical analysis of individual Si nanowires shows that with a larger diameter there is an increasing differential stress associated with the differential volume expansion due to lithiation, which proceeds radially inward. [52-54,89,100-103] Thicker films of Si will also be liable to fracture more both normal to the substrate plane [89] and in parallel to the substrate - film interface. [93-95] Since both Si and Ge cycled specimens are fully amorphous in their delithiated state, the behavior of Ge wires and films is expected to be qualitatively similar. This is different from cycle 1 lithiation, where Ge lithiates more isotropically than Si, as discussed. Figures 6(c) and 6(d) show the relationship between the coulombic efficiency (at cycle 50) and the wire diameter and film thickness. There again is a strong negative trend with progressively worsening CE with larger wire and film thicknesses. It is known that cycling CE is degraded by a combination of progressive SEI formation with every cycle and any loss of active material that contains Li. The second aspect may be understood in terms of a partially lithiated section of a nanowire fracturing from the assembly. As will be demonstrated in the next series of figures, at the thicker dimensions both mechanisms do contribute to the loss of CE. Figure 6(e) and 6(f) show the (less strong) trend of both capacity retention and CE decreasing with increasing mean nanowire length. This is presumably due to a higher statistical chance of catastrophic fracture occurring in longer wires.

Figure 7 compares the morphology of the post-cycled 0.12mg-(320/2min) and 0.2mg-(360/2min) specimens. With cycling, both electrodes show progressive lithiation-induced "stranding" of the nanowires, agreeing with previous reports on a range of cycled Ge

nanostructures. [35,39,41]. Figure 8 shows the HAADF images and overlaid EELS maps of Ge, Li, C, and O for the post-100 cycles specimens in their delithiated state. For this analysis we found non-agglomerated nanowires, which were usually located near the top surface of the electrode. Figure 8(a) shows the 0.12mg-(320/2min) specimens, 8(b) shows the 0.73mg-(320/10min) specimens, and 8(c) shows the 0.2mg-(360/2min) specimens. In all three cases the microstructure of the individual cycled GeNWs is analogous: The nanowires have undergone substantial stranding parallel to their longitudinal direction and are now interspersed with visible porosity also running lengthwise (marked by arrows in the first panel of each series). The formation of nanopores during consecutive lithiation/delithiation has been previously reported for Ge nanowires. [52,58] Each of the newly exposed Ge surfaces is covered by SEI, which shows up as strong C, O and Li signals.

Figures 9 (a) and (b) show FIB cross-section SEM images of the post-100 cycles 0.73mg-(320/10min) and 0.86mg-(360/10min) electrodes. Near the current collector base (unlike near the top) the post-cycled nanowires are heavily agglomerated with SEI. There is much more cracking at the film - current collector interface in the 0.86mg-(360/10min) electrode. The stress driven failure of the bulk thin film has been discussed already. As the parasitic Ge film fractures during lithiation/delithiation cycling there is fresh Ge is exposed to the electrolyte. This promotes more SEI growth, adding to the overall film stress and reducing the CE. The analytical maps shown in Figures 9(c) and 9(d) highlight the enhanced SEI formation near the nanowire – current collector interface, where a higher C and O signal is observed in that region. Note that heavier elements in the steel substrate and the W in the "surface cap" have a large number of emission lines that overlap with any of the lighter elements and thus appear bright in all of the maps. The cycling-

induced overgrowth of SEI on each nanowire also adds to the total film stress as there are regions were there is so much SEI that the nanowires actually fuse together to make a nanoporous composite.

Electrochemical impedance spectroscopy (EIS) was employed to further understand the effect of mass loading on the cycling performance. Button cells (2 electrode) were tested in their delithiated state immediately after cycling. The Nyquist plots in Figure 10 are for the post-cycled electrodes, analyzed after cycle 10 and 100 delithiation. The insert in the figures shows the equivalent circuits employed for modeling. The spectra exhibit well-defined features including a high-frequency depressed semi-circle, followed by a 45° sloped line in the low-frequency region of the spectra. The intercept of the spectra with the real part of the impedance axis shows equivalent series resistance (R_{es}) of the half-cell. The diameter of the high frequency semi-circle represents the interfacial charge transfer resistance (R_{ct}). [104] At cycle 10 the equivalent series and the charge transfer resistances of all the specimens are on par: R_{es} is 4, 5, 6 and 10 Ω for the 0.12mg-(320/2min), 0.2mg-(360/2min), 0.73mg-(320/10min), and 0.86 mg-(360/10min), respectively. In the same order R_{ct} is 90, 70, 80 and 60 Ω. Cycling has a negative effect on the higher mass loaded specimens. After 100 cycles R_{es} is 4.5, 5, 22 and 19 Ω for the 0.12mg-(320/2min), 0.2mg-(360/2min), 0.73mg-(320/10min), and 0.86 mg-(360/10min), respectively. R_{ct} increases to 80, 240, 180 and 340 Ω. The R_{ct} in post-cycled LIB anodes is known to be related to the charge transfer resistance through the multilayer SEI structure that forms initially upon cycle 1 lithiation and subsequently during cycling as fresh electrode material is exposed to the electrolyte. [108-105] For a given material, higher values of R_{ct} are considered synonymous with more interfaces that impede Li ion transfer into the bulk of the electrode, caused by a thicker

SEI. [109] Since SEI irreversibly consumes Li during the reduction process, higher rates of SEI formation lead to lower CE values since Li is irreversibly consumed. Increasing R_{es} may be associated with a degradation of the electrical conductivity of the electrode materials, in addition to other factors such as an increasing interfacial electrical resistance, an increasing resistance of the current collector and of the electrochemical fixtures (the last two effects are unlikely). Having the specimens R_{ct} values be on-par at cycle 10 agrees with the results in Figure 5, showing on-par retained capacity and a similar CE at that point. After 100 cycles EIS results also agree with the cycling data, with the CE at cycle 100 being the lowest for the 0.86 mg-(360/10min) specimens and the best for 0.12mg-(320/2min) electrodes.

Figure 11 shows the XPS data for all the 0.12mg-(320/2min) electrodes after 1, 10 and 100 cycles. In the C 1s spectra, the shoulder off the main hydrocarbon signal at about 286 – 287 eV is attributed to polyethylene oxide (PEO). Lithium ethylene dicarbonate peak in C 1s appears as a broad shoulder at the binding energy of 288 – 289 eV. The peak associated with the Li_2CO_3 is located at about 290 eV. The O 1s spectra confirm the assignments made for C 1s spectra. The maximum intensity has a binding energy of around 531 – 532 eV for all the materials with a broad shoulder at higher binding energy of 532 – 534 eV. The main peak at ~ 531.5 eV represents Li_2CO_3 compound and the broad shoulder off the main carbonate signal at around 532 – 533 eV is associated with the PEO-like polymers and lithium ethylene dicarbonate. Presence of fluorine and phosphorous in the SEI film suggests that degradation of $LiPF_6$ salt occurred during cycling. LiF is the main compound formed upon degradation of $LiPF_6$ through either a chemical decomposition or a reaction in presence of water. Li 1s spectra also have a main peak with a center at 55.2 eV, corresponding to Li_2CO_3, and a shoulder at about 56 eV, for LiF.

Correspondingly, the main peak in F 1s spectra at ~ 684.5 eV is assigned to LiF. [110] The main signal in P 2p is from $Li_xPF_yO_z$, produced from the reaction of PF_5, formed upon chemical decomposition of $LiPF_6$ salt, with the contaminations and compounds in the cell. The XPS measurements indicate that the SEI layer consists mostly of Li_2CO_3 and LiF compounds. Li_2CO_3 is a well-known electrolyte reduction product, [111,112] the irreversible formation of which is associated with poor coulombic efficiency. Lithium carbonate, Li_2CO_3, and lithium ethylene dicarbonate, $(CH_2OCO_2Li)_2$, are produced upon the electrochemical reduction of EC solvent. Polyethylene oxide (PEO), $-(CH_2CH_2O)_n-$, is another product of EC degradation. [110] LiF is considered an electroless decomposition product of the $LiPF_6$ salt that forms over time. [107,113]

Figures 12 (a) – (c) show TOF-SIMS depth profiles of Li and Fe concentration through the thickness of three pure Ge films that were sputtered onto stainless steel substrates and then lithiated twice. The films had thicknesses of 150, 300 and 500 nm and were employed as model systems for understanding Li segregation in the Ge parasitic films present in the nanowire arrays. The Fe signal originates from the stainless steel current collector and demarcates the current collector – electrode interface. The profiles reveal Li segregation to the current collector interface in the 300 and 500 nm specimens, but with negligible segregation present in the 150 nm electrode. Segregation in the 500 nm specimen appears to be stronger than in the 300 nm film. The actual Li segregation profile in the 300 and 500 nm samples is probably sharper than what the TOF-SIMS results indicate, since the current collector's inherent roughness will smear the through-thickness Fe and Li distributions. The results shown in Figure 12 are the first direct experimental confirmation of this phenomenon in regard to Ge electrodes. Our group has recently reported a similar interfacial segregation behavior of Na in Sn films deposited on

stainless steel current collectors. [70] Authors reported calculations demonstrating that lithiation of pure Sn and Si leads to elastic softening of Sn-Li [114] and Si-Li [115] phases. Moreover failure of similar "film-on-support" type architectures (Si on Cu) has been both experimentally and theoretically proven to be critically related to a weakening of the mutual interface due to Li segregation and a change in bonding of the Si-Li alloy. [66] It is reasonable to expect an analogous effect for Ge-Li. Such phenomenology would further explain our electrochemical cycling and FIB results, where the array with a higher parasitic film thickness and hence with potentially more severe Li segregation is the one showing more interfacial fracture.

Finally, it is instructive to compare our electrochemical testing results with state-of-the-art scientific literature concerning the electrochemical performance of a range of Ge - based nanostructures employed as LIB anodes. Table 3 presents this comparison, highlighting the essential features of each material including the initial CE, reversible capacity at cycle 1 and at cycle 100, a steady-state cycling CE, and the high rate capability. In the Table, we present the performance of our best nanowire arrays, i.e. the ones with 0.12 mg mass loading. It may be observed that the performance of this electrode is among the best in all respects as compared to a range of advanced Ge - based nanostructures.

Table 3: A comparison of our best-performing electrode with previously published literature on Ge-based LIB anodes.

Electrodes	**Initial Coulombic Efficiency (%)**	**Cycling Capacity $mAhg^{-1}$ (current density)**		**Coulombic Efficiency (%) (current density)**		**Rate Capability $mAhg^{-1}$ (current density)**
		10^{st}	**100^{th}**	**10^{th}**	**100^{th}**	

0.12mg-(320°C/2min)	*95*	*1318*	*1405*	*99.85*	*99.86*	*1143*
	(138 mAg^{-1})	*(138 mAg^{-1})*	*(138 mAg^{-1})*	*(138 mAg^{-1})*	*(138 mAg^{-1})*	*(6900 mAg^{-1})*
	(0.1C)	*(0.1C)*	*(0.1C)*	*(0.1C)*	*(0.1C)*	*(5C)*
Alkanethiol-Passivated	79.3	1300	1150	N/A	~99	733
Ge Nanowires[41]	(0.1C)	(0.1C)	(0.1C)		(0.1C)	(6.5C)
Cu–Ge core–shell	80.1	~1538	NA	~97	NA	1103
nanowire arrays [81]	(800 mAg^{-1})	(800 mAg^{-1})		(800 mAg^{-1})		(6400 mAg^{-1})
Ge nanoparticle–	~33	~875	~850	~94	~97	~500
multiwalled CNT [116]	(1623 mAg^{-1})	(1623 mAg^{-1})	(1623 mAg^{-1})	(1623 mAg^{-1})	(1623 mAg^{-1})	(8115 mAg^{-1})
Carbon-Coated Ge	~90	~500	NA	NA	NA	NA
Composite [11]	(100 mAg^{-1})	(100 mAg^{-1})				
Graphene-Supported	~81	~830	~375	~93	~98	~100
Germanium [42]	(0.05C)	(0.05C)	(0.1C)	(0.05C)	(0.1C)	(1C)
Entangled Ge NWs and	78	~ 1200	NA	~99		~600
Graphite Nanofibers[55]	(0.1C)	(0.1C)		(0.1C)		(5C)
Ge Nanotubes [117]	76	~900	NA	~99	NA	~650
	(0.2C)	(0.2C)		(0.2C)		(5C)
Ge nanowires-based	62.1	~900	NA	N/A	NA	~600
carbon composite[38]	(160 mAg^{-1})	(160 mAg^{-1})				(800 mAg^{-1})
Germanium–Graphene	~80	~800	~720	~99	~99.5	~300
composite [30]	(400 mAg^{-1})	(400 mAg^{-1})	(400 mAg^{-1})	(400 mAg^{-1})	(400 mAg^{-1})	(5000 mAg^{-1})
Ge Nanowires [40]	39	~1150	NA	~99	NA	~600
	(0.05C)	(0.05C)		(0.05C)		(2C)
Ge nanowire anode	91	~800	~700	NA	~90	~700
sheathed with carbon [39]	(0.5C)	(0.5C)	(0.5C)		(0.5C)	(6C=4800 mAg^{-1})
Ge Nanoparticles [23]	96	NA	NA	NA	NA	NA
Hybrid Ge Nanoparticle	~58	NA	NA	NA	NA	~300
Single-Wall CNT [23]	(50 mAg^{-1})					(2000 mAg^{-1})
Ge@C Core−Shell	~52	~1025	NA	~99	NA	~380
Nanoparticles and	(50 mAg^{-1})	(50 mAg^{-1})		(50 mAg^{-1})		(3600 mAg^{-1})
Graphene Networks [10]						
Mesoporous Ge [24]	43.8	~900	NA	NA	NA	NA
	(150 mAg^{-1})	(150 mAg^{-1})				
Ge Thin Films[18]	~33	~1700	NA	~97	NA	~500
	(375 mAg^{-1})	(375 mAg^{-1})		(375 mAg^{-1})		(1000C)
Ion-beam Modified Ge	98.4	1300	1342	~96	~95	1000
Films [100]	(0.14C)	(0.14C)	(0.14C)	(0.14C)	(0.14C)	(1.1C)

Solution-Grown Ge Nanowires [8]	~82 (0.1C)	~1300 (0.1C)	~ 1400 (0.1C)	~97 (0.1C)	~99 (0.1C)	~800 (5C)
p- and n-doped Ge Thin films [17]	NA	~750 (μAh cm^{-2}. μm^{-1}) (100 μA cm^{-2})	~800 (μAh cm^{-2}.μm^{-1}) (100 μA cm^{-2})	NA	NA	~800 (mAh.g^{-1}) (1600 μA cm^{-2})
Ge/Cu_3Ge/C composite[22]	78.4 (100 mAg^{-1})	~1000 (100 mAg^{-1})	NA	N/A	NA	NA
GeO_2/Ge/C Nanocomposite [5]	82 (0.05C)	~1800 (1C=2100 mAg^{-1})	NA	NA	NA	~1750 (5C)
Colloidal Tin-Germanium Nanorods [6]	~52 (1000 mAg^{-1})	~1650 (1000 mAg^{-1})	~1500 (1000 mAg^{-1})	NA	NA	~750 (4000 mAg^{-1})
GeO_2−SnCoC Composite[7]	80 (100 mAg^{-1})	~950 (300 mAg^{-1})	~800 (300 mAg^{-1})	NA	NA	~500 (1200 mAg^{-1})
Ge.Mo Composite [99]	91.6	~1050	~930	>99	97.2	NA
Ge Thin Film [99]	~95 (167 μA cm^{-2})	~1020 (167 μA cm^{-2})	~720 (167 μA cm^{-2})	~99 (167 μA cm^{-2})	~97 (167 μA cm^{-2})	NA
Ge Nanowire Arrays [35]	97 (0.5C)	~1120 (0.5C)	~1000 (0.5C)	~97 (0.5C)	~98 (0.5C)	~700 (5C)
Graphene-encapsulated Ge Nanowires [36]	~53	~1400	NA	~96	NA	~1000
Metallic Ge [36]	~72 (1C=1600mAg^{-1})	~300 (1600 mAg^{-1})	NA	~99 (1600 mAg^{-1})	NA	NA (8000 mAg^{-1})
Ge Thin Film [20]	~65 (0.1C)	~1250 (0.1C)	NA	NA	NA	~1130 (5C)
Sn–Ge alloy[32]	~78 (0.1C)	~1100 (0.1C)	NA	~98 (0.1C)	NA	~500 (5C)
GeS Nanocrystals [12]	78	~1375	~1250	~99	~99	~1125
GeO_2 Nanocrystals [12]	70	~1300	~1120	~99	~99	~625
Ge Nanocrystals [12]	70 (0.1C)	~1250 (0.1C)	~1125 (0.1C)	~98.5 (0.1C)	~98.5 (0.1C)	~600 (5C)
Ge microstructures [50]	NA	~550 (0.05C)	NA	~98 (0.05C)	NA	NA

Conclusions

Diverse germanium nanowire arrays were synthesized by VLS growth for 2, 5 and 10 minutes at 320°C or 360°C. We demonstrate a strong empirical correlation between the mass loading and the electrodes' electrochemical performance, which converged the 320°C and 360°C results into one relatively narrow band. There is a degradation of cycling capacity retention, coulombic efficiency and rate capability with higher mass loading and with coarser array geometry (mean nanowire diameter, mean thickness of the parasitic Ge films at the current collector - array interface). The inferior cycling capacity retention and CE is correlated with increasing levels of Li segregation to the current collector interface, and to preferential SEI formation and macroscopic cracking in that region. The inferior rate capability is likely caused by the longer Li diffusion distances associated with the larger diameters of the nanowires, and with the thicker Ge films at the bottom of the arrays. Our findings may serve as a useful design tool for fabricating high performance 1-D nanostructured anodes for Li ion storage applications.

Acknowledgment

This work was sponsored by NSERC Discovery.

References

1 B. Dunn, H. Kamath and J. M. Tarascon, *Science*, 2011, **334**, 928-935.

2 J. M. Tarascon and M. Armand, *Nature*, 2001, **414**, 359-367.

3 P. V. Braun, J. Cho, J. H. Pikul, W. P. King and H. G. Zhang, *Curr. Opin. Solid State Mater. Sci.*, 2012, **16**, 186-198.

4 N. Ding, J. Xu, Y. X. Yao, G. Wegner, X. Fang, C. H. Chen and I. Lieberwirth, *Solid State Ionics*, 2009, **180**, 222-225.

5 K. H. Seng, M.-h. Park, Z. P. Guo, H. K. Liu and J. Cho, *Nano Lett.*, 2013, **13**, 1230-1236.

6 M. I. Bodnarchuk, K. V. Kravchyk, F. Krumeich, S. Wang and M. V. Kovalenko, *ACS nano*, 2014, **8**, 2360-2368.

7 B. Liu, A. Abouimrane, M. Balasubramanian, Y. Ren and K. Amine, *J. Phys. Chem. C*, 2014, **118**, 3960-3967.

8 A. M. Chockla, K. C. Klavetter, C. B. Mullins and B. A. Korgel, *Acs Appl. Mater. & Interfaces*, 2012, **4**, 4658-4664.

9 C. S. Fuller and J. C. Severiens, *Phys. Rev.*, 1954, **96**, 21-24.

10 D. J. Xue, S. Xin, Y. Yan, K. C. Jiang, Y. X. Yin, Y. G. Guo and L. J. Wan, *J. Am. Chem. Soc.*, 2012, **134**, 2512-2515.

11 S. Yoon, C. M. Park and H. J. Sohn, *Electrochem. Solid State Lett.*, 2008, **11**, A42-A45.

12 Y. J. Cho, H. S. Im, H. S. Kim, Y. Myung, S. H. Back, Y. R. Lim, C. S. Jung, D. M. Jang, J. Park, E. H. Cha, W. Il Cho, F. Shojaei and H. S. Kang, *Acs Nano*, 2013, **7**, 9075-9084.

13 Y.Yu, C.Yue, S. Sun, W. Lin, H. Su, B. Xu, J. Li, S. Wu, J. Li, and J. Kang, *ACS Appl. Mater. Interfaces*, 2014, **6(8)**, 5884-90.

14 C. K. Chan, H. L. Peng, G. Liu, K. McIlwrath, X. F. Zhang, R. A. Huggins and Y. Cui, *Nature Nanotech.*, 2008, **3**, 31-35.

15 A. H. Whitehead, K. Edstrom, N. Rao and J. R. Owen, *J. Power Sources*, 1996, **63**, 41-45.

16 L. Baggetto, E. J. M. Hensen and P. H. L. Notten, *Electrochimica Acta*, 2010, **55**, 7074-7079.

17 B. Laforge, L. Levan-Jodin, R. Salot and A. Billard, *J. Electrochem. Soc.*, 2008, **155**, A181-A188.

18 J. Graetz, C. C. Ahn, R. Yazami and B. Fultz, *J. Electrochem. Soc.*, 2004, **151**, A698-A702.

19 N. G. Rudawski, B. L. Darby, B. R. Yates, K. S. Jones, R. G. Elliman and A. A. Volinsky, *Appl. Phys. Lett.*, 2012, **100**.

20 P. R. Abel, A. M. Chockla, Y.-M. Lin, V. C. Holmberg, J. T. Harris, B. A. Korgel, A. Heller and C. B. Mullins, *Acs Nano*, 2013, **7**, 2249-2257.

21 X. Liu, J. Zhao, J. Hao, B.-L. Su and Y. Li, *J. Mater. Chem. A*, 2013, **1**, 15076-15081.

22 Y. Hwa, C. M. Park, S. Yoon and H. J. Sohn, *Electrochimica Acta*, 2010, **55**, 3324-3329.

23 R. A. DiLeo, S. Frisco, M. J. Ganter, R. E. Rogers, R. P. Raffaelle and B. J. Landi, *J. Phys. Chem. C*, 2011, **115**, 22609-22614.

24 L. C. Yang, Q. S. Gao, L. Li, Y. Tang and Y. P. Wu, *Electrochem. Commun.*, 2010, **12**, 418-421.

25 Y. Son, M. Park, J. S. Lee, J. H. Jang, Y. Kim and J. Cho, *Nano Lett.*, 2014, **14**, 1005-1010.

26 T. Song, Y. Jeon, M. Samal, H. Han, H. Park, J. Ha, D. K. Yi, J.-M. Choi, H. Chang, Y.-M. Choi and U. Paik, *Energ. Environ. Sci.*, 2012, **5**, 9028-9033.

27 W. Li, Z. Yang, J. Cheng, X. Zhong, L. Gu, Y. Yu, *Nanoscale*, 2014, **6**, 4532.

28 W. Li, J. Zheng, T. Chen, T. Wang, X. Wang and X. Li, *Chem. Commun.*, 2014, **50**, 2052-2054.

29 C. Zhong, J.-Z. Wang, X.-W. Gao, D. Wexler and H.-K. Liu, *J. Mater. Chem. A*, 2013, **1**, 10798-10804.

30 J.-G. Ren, Q-H. Wu, H. Tang, G. Hong, W. Zhang, and S.-T. Lee*, J. Mater. Chem. A*, 2013, **1**, 1821.

31 M. H. Park, Y. Cho, K. Kim, J. Kim, M. L. Liu and J. Cho, *Angewandte Chemie-International Edition*, 2011, **50**, 9647-9650.

32 S. Fan, L. Y. Lim, Y. Y. Tay, S. S. Pramana, X. Rui, M. K. Samani, Q. Yan, B. K. Tay, M. F. Toney and H. H. Hng, *J. Mater. Chem. A*, 2013, **1**, 14577-14585.

33 Y. J. Cho, C. H. Kim, H. S. Im, Y. Myung, H. S. Kim, S. H. Back, Y. R. Lim, C. S. Jung, D. M. Jang, J. Park, S. H. Lim, E. H. Cha, K. Y. Bae, M. S. Song and W. Il Cho, *Phys. Chem. Chem. Phys.*, 2013, **15**, 11691-11695.

34 T. Song, H. Cheng, K. Town, K. Park, R. W. Black, S. Lee, W. Park, Y. Huang, J. A. Rogers, L. F. Nazar, and U. Paik. *Adv. Funct. Mater.,* 2014, **24**, 1458–1464.

35 T. Kennedy, E. Mullane, H. Geaney, M. Osiak, C. O'Dwyer and K. M. Ryan, *Nano Lett.*, 2014, **14**, 716-723.

36 C. Wang, J. Ju, Y. Yang, Y. Tang, J. Lin, Z. Shi, R. P. S. Han and F. Huang, *J. Mater. Chem. A*, 2013, **1**, 8897-8902.

37 D. D. Vaughn and R. E. Schaak, *Chem. Soc. Rev.*, 2013, **42**, 2861-2879.

38 L. P. Tan, Z. Y. Lu, H. T. Tan, J. X. Zhu, X. H. Rui, Q. Y. Yan and H. H. Hng, *J. Power Sources*, 2012, **206**, 253-258.

39 M. H. Seo, M. Park, K. T. Lee, K. Kim, J. Kim and J. Cho, *Energ. Environ. Sci.*, 2011, **4**, 425-428.

40 C. K. Chan, X. F. Zhang and Y. Cui, *Nano Lett.*, 2008, **8**, 307-309.

41 F. W. Yuan, H. J. Yang and H. Y. Tuan, *Acs Nano*, 2012, **6**, 9932-9942.

42 A. M. Chockla, M. G. Panthani, V. C. Holmberg, C. M. Hessel, D. K. Reid, T. D. Bogart, J. T. Harris, C. B. Mullins and B. A. Korgel, *J. Phys. Chem. C*, 2012, **116**, 11917-11923.

43 Y. Liu, S. Zhang and T. Zhu, *Chem.Electro. Chem.,* 2014*,* **1**, 817.

44 B. A. Korgel, *J. Phys. Chem. Lett.*, 2014, **5**, 749-750.

45 W. J. Zhang, *J. Power Sources*, 2011, **196**, 13-24.

46 D. Aurbach, B. Markovsky, G. Salitra, E. Markevich, Y. Talyossef, M. Koltypin, L. Nazar, B. Ellis and D. Kovacheva, *J. Power Sources*, 2007, **165**, 491-499.

47 Y. Matsumura, S. Wang and J. Mondori, *J. Electrochem. Soc.*, 1995, **142**, 2914-2918.

48 A. Kohandehghan, P. Kalisvaart, M. Kupsta, B. Zahiri, B. S. Amirkhiz, Z. P. Li, E. L. Memarzadeh, L. A. Bendersky and D. Mitlin, *J. Mater. Chem. A*, 2013, **1**, 1600-1612.

49 H. Wu, G. Chan, J. W. Choi, I. Ryu, Y. Yao, M. T. McDowell, S. W. Lee, A. Jackson, Y. Yang, L. B. Hu and Y. Cui, *Nature Nanotech.*, 2012, **7**, 309-314.

50 B. R. Long, J. L. Goldman, R. G. Nuzzo and A. A. Gewirth, *J. Solid State Electrochem.*, 2013, **17**, 3015-3020.

51 Y. Liu, X. H. Liu, B.-M. Nguyen, J. Yoo, J. P. Sullivan, S. T. Picraux, J. Y. Huang and S. A. Dayeh, *Nano Lett.*, 2013, **13**, 4876-4883.

52 X. H. Liu, Y. Liu, A. Kushima, S. L. Zhang, T. Zhu, J. Li and J. Y. Huang, *Adv. Energy Mater.*, 2012, **2**, 722-741.

53 X. H. Liu and J. Y. Huang, *Energ. Environ. Sci.*, 2011, **4**, 3844-3860.

54 X. H. Liu, H. Zheng, L. Zhong, S. Huan, K. Karki, L. Q. Zhang, Y. Liu, A. Kushima, W. T. Liang, J. W. Wang, J. H. Cho, E. Epstein, S. A. Dayeh, S. T. Picraux, T. Zhu, J. Li, J. P. Sullivan, J. Cumings, C. S. Wang, S. X. Mao, Z. Z. Ye, S. L. Zhang and J. Y. Huang, *Nano Lett.*, 2011, **11**, 3312-3318.

55 S. H. Woo, S. J. Choi, J. H. Park, W. S. Yoon, S. W. Hwang and D. Whang, *J. Electrochem. Soc.*, 2013, **160**, A112-A116.

56 Y. Yao, M. T. McDowell, I. Ryu, H. Wu, N. A. Liu, L. B. Hu, W. D. Nix and Y. Cui, *Nano Letters*, 2011, **11**, 2949-2954.

57 N. S. Choi, Y. Yao, Y. Cui and J. Cho, *Journal of Materials Chemistry*, 2011, **21**, 9825-9840.

58 X. H. Liu, S. Huang, S. T. Picraux, J. Li, T. Zhu and J. Y. Huang, *Nano Lett.*, 2011, **11**, 3991-3997.

59 J. H. Cho and S. T. Picraux, *Nano Lett.*, 2013, **13**, 5740-5747.

60 H. Adhikari, A. F. Marshall, C. E. D. Chidsey and P. C. McIntyre, *Nano Lett.*, 2006, **6**, 318-323.

61 A. Rath, J. K. Dash, R. R. Juluri, A. Ghosh, T. Grieb, M. Schowalter, F. F. Krause, K. Muller, A. Rosenauer and P. V. Satyam, *Cryst. Eng. Comm*, 2014, **16**, 2486-2490.

62 J. L. Taraci, T. Clement, J. W. Dailey, J. Drucker and S. T. Picraux, *Nucl. Instrum. Methods Phys. Res., Sect. B -Beam Interactions with Materials and Atoms*, 2006, **242**, 205-208.

63 H. Adhikari, P. C. McIntyre, A. F. Marshall and C. E. D. Chidsey, *J. Appl. Phys.*, 2007, **102**.

64 M. Simanullang, K. Usami, T. Kodera, K. Uchida and S. Oda, *Jpn. J. Appl. Phys.*, 2011, **50**.

65 Y. Sierra-Sastre, S. A. Dayeh, S. T. Picraux and C. A. Batt, *Acs Nano*, 2010, **4**, 1209-1217.

66 M. E. Stournara, X. Xiao, Y. Qi, P. Johari, P. Lu, and B. W. Sheldon, *Nano Lett.*, 2013, **13**, 4759−4768.

67 D. Santhanagopalan, D. Qian, T. McGilvray, Z. Y. Wang, F. Wang, F. Camino, J. Graetz, N. Dudney and Y. S. Meng, *Journal of Physical Chemistry Letters*, 2014, **5**, 298.

68 J.-T. Li, J. Swiatowska, A. Seyeux, L. Huang, V. Maurice, S.-G. Sun and P. Marcus, *Journal of Power Sources*, 2010, **195**, 8251.

69 J.-T. Li, J. Swiatowska, V. Maurice, A. Seyeux, L. Huang, S.-G. Sun and P. Marcus, *Journal of Physical Chemistry C*, 2011, **115**, 7012.

70 B.Farbod, C. Kai, W. P. Kalisvaart, M. Kupsta, B. Zahiri, A. Kohandehghan, E. Memarzadeh, Z. Li, E. J. Luber, and D. Mitlin, ACS Nano, 2014, DOI: 10.1021/nn4063598.

71 H. Adhikari, A. F. Marshall, I. A. Goldthorpe, C. E. D. Chidsey and P. C. McIntyre, *ACS Nano*, 2007, **1**, 415-422.

72 L. Zhang, C. M. B. Holt, E. Luber, B. C. Olsen, H. Wang, M. Danaie, X. Cui, X. Tan, V. Lui, W. P. Kalisvaart, and D. Mitlin, *J. Phys. Chem. C,* 2011, **115**, 24381–24393.

73 C. O'Regan, S. Biswas, N. Petkov and J. D. Holmes, *J. Mater. Chem. C*, 2014, **2**, 14-33.

74 C. Renard, R. Boukhicha, C. Gardes, F. Fossard, V. Yam, L. Vincent, D. Bouchier, S. Hajjar, J. L. Bubendorff, G. Garreau and C. Pirri, *Thin Solid Films*, 2012, **520**, 3314-3318.

75 T. I. Kamins, X. Li and R. S. Williams, *Nano Lett.*, 2004, **4**, 503-506.

76 S. Kodambaka, J. Tersoff, M. C. Reuter and F. M. Ross, *Science*, 2007, **316**, 729-732.

77 C. B. Li, K. Usami, H. Mizuta and S. Oda, *J. Appl. Phys.*, 2009, **106**.

78 J. B. Hannon, S. Kodambaka, F. M. Ross and R. M. Tromp, *Nature*, 2006, **440**, 69-71.

79 J. H. Kim, S. R. Moon, Y. Kim, Z. G. Chen, J. Zou, D. Y. Choi, H. J. Joyce, Q. Gao, H. H. Tan and C. Jagadish, *Nanotech.*, 2012, **23**.

80 L. Baggetto and P. H. L. Notten, *J. Electrochem. Soc.*, 2009, **156**, A169-A175.

81 J. Z. Wang, N. Du, H. Zhang, J. X. Yu and D. R. Yang, *J. Mater. Chem.*, 2012, **22**, 1511-1515.

82 E. L. Memarzadeh, W. P. Kalisvaart, A. Kohandehghan, B. Zahiri, C. M. B. Holt and D. Mitlin, *J. Mater. Chem.*, 2012, **22**, 6655-6668.

83 P. K. E.L. Memarzadeh, K. Cui, A. Kohandehghan, M. Kupsta, B. Olsen, D. Mitlin, *Phys. Chem. Chem. Phys.*, 2013, p. **13646**.

84 A. Mukhopadhyay and B. W. Sheldon, *Progress in Mater. Sci.,* 2014, **63**, 58–116.

85 X. Su, Q. L. Wu, J. C. Li, X. C. Xiao, A. Lott, W. Q. Lu, B. W. Sheldon and J. Wu, *Adv. Energ. Mater.*, 2014, **4**.

86 X. H. Liu, L. Zhong, S. Huang, S. X. Mao, T. Zhu and J. Y. Huang, *Acs Nano*, 2012, **6**, 1522-1531.

87 H. Kim, M. Seo, M. H. Park and J. Cho, *Angewandte Chemie-International Edition*, 2010, **49**, 2146-2149.

88 M. T. McDowell, S. W. Lee, J. T. Harris, B. A. Korgel, C. M. Wang, W. D. Nix and Y. Cui, *Nano Lett.*, 2013, **13**, 758-764.

89 I. Ryu, J. W. Choi, Y. Cui and W. D. Nix, *J. Mech. Phys. Solids*, 2011, **59**, 1717-1730.

90 S. W. Lee, M. T. McDowell, L. A. Berla, W. D. Nix and Y. Cui, *Proceedings of the National Academy of Sciences of the United States of America*, 2012, **109**, 4080-4085.

91 X. Xiao, P. Liu, M. W. Verbrugge, H. Haftbaradaran and H. Gao, *J. Power Sources*, 2011, **196**, 1409-1416.

92 S. K. Soni, B. W. Sheldon, X. C. Xiao and A. Tokranov, *Scripta Materialia*, 2011, **64**, 307-310.

93 H. Haftbaradaran, X. C. Xiao, M. W. Verbrugge and H. J. Gao, *J. Power Sources*, 2012, **206**, 357-366.

94 H. Haftbaradaran and H. J. Gao, *Appl. Phys. Lett.*, 2012, **100**.

95 H. Haftbaradaran, X. C. Xiao and H. J. Gao, *Modell. Simul. Mater. Sci. Eng.*, 2013, **21**.

96 W. Liang, H. Yang, F. Fan, Y. Liu, X. H. Liu, J. Y. Huang, T. Zhu and S. Zhang, *Acs Nano*, 2013, **7**, 3427-3433.

97 E. M. Lotfabad, P. Kalisvaart, A. Kohandehghan, K. Cui, M. Kupsta, B. Farbod and D. Mitlin, *J. Mater. Chem. A*, 2014, **2**, 2504-2516.

98 A. Kohandehghan, P. Kalisvaart, K. Cui, M. Kupsta, E. Memarzadeh and D. Mitlin, *J. Mater. Chem. A*, 2013, **1**, 12850-12861.

99 C. M. Hwang and J. W. Park, *Thin Solid Films*, 2010, **518**, 6590-6597.

100 S. T. Boles, A. Sedlmayr, O. Kraft and R. Monig, *Appl. Phys. Lett.*, 2012, **100**.

101 T. T. Fister, J. L. Goldman, B. R. Long, R. G. Nuzzo, A. A. Gewirth and P. A. Fenter, *Appl. Phys. Lett.*, 2013, **102**.

102 S. P. V. Nadimpalli, V. A. Sethuraman, S. Dalavi, B. Lucht, M. J. Chon, V. B. Shenoy and P. R. Guduru, *J. Power Sources*, 2012, **215**, 145-151.

103 R. Deshpande, Y. T. Cheng and M. W. Verbrugge, *J. Power Sources*, 2010, **195**, 5081-5088.

104 M. D. Levi and D. Aurbach, J. *Phys. Chem. B*, 1997, **101**, 4630-4640.

105 V. Etacheri, U. Geiger, Y. Gofer, G. A. Roberts, I. C. Stefan, R. Fasching and D. Aurbach, *Langmuir*, 2012, **28**, 6175-6184.

106 E. Pollak, G. Salitra, V. Baranchugov and D. Aurbach, *J. Phys. Chem. C*, 2007, **111**, 11437-11444.

107 K. Xu, *Chem. Rev.*, 2004, **104**, 4303-4417.

108 J. C. Guo, A. Sun, X. L. Chen, C. S. Wang and A. Manivannan, *Electrochimica Acta*, 2011, **56**, 3981-3987.

109 N. Ding, J. Xu, Y. X. Yao, G. Wegner, I. Lieberwirth and C. H. Chen, *J. Power Sources*, 2009, **192**, 644-651.

110 B. Philippe, R. Dedryvère, M. Gorgoi, H. Rensmo, D. Gonbeau, and K. Edström. Chem. Mater., 2013, **25**, 394–404.

111 D. Aurbach, B. Markovsky, M. D. Levi, E. Levi, A. Schechter, M. Moshkovich and Y. Cohen, *J. Power Sources*, 1999, **81**, 95-111.

112 K. W. Schroder, H. Celio, L. J. Webb and K. J. Stevenson, *J. Phys. Chem. C*, 2012, **116**, 19737-19747.

113 D. Aurbach, E. Zinigrad, Y. Cohen and H. Teller, *Solid State Ionics*, 2002, **148**, 405-416.

114 M. E. Stournara, P. R. Guduru and V. B. Shenoy, *J. Power Sources*, 2012, **208**, 165-169.

115 V. B. Shenoy, P. Johari and Y. Qi, *J. Power Sources*, 2010, **195**, 6825-6830.

116 I-S. Hwang, J-C. Kim,b S-D. Seo, S. Lee, J-H. Lee and D-W. Kim, *Chem. Commun.,* 2012, 48, 7061–7063.

117 M-H. Park, Y.H. Cho, K. Kim, J. Kim, M. Liu, and J. Cho, *Angew. Chem. Int. Ed.*, 2011, 50, 9647 –9650.

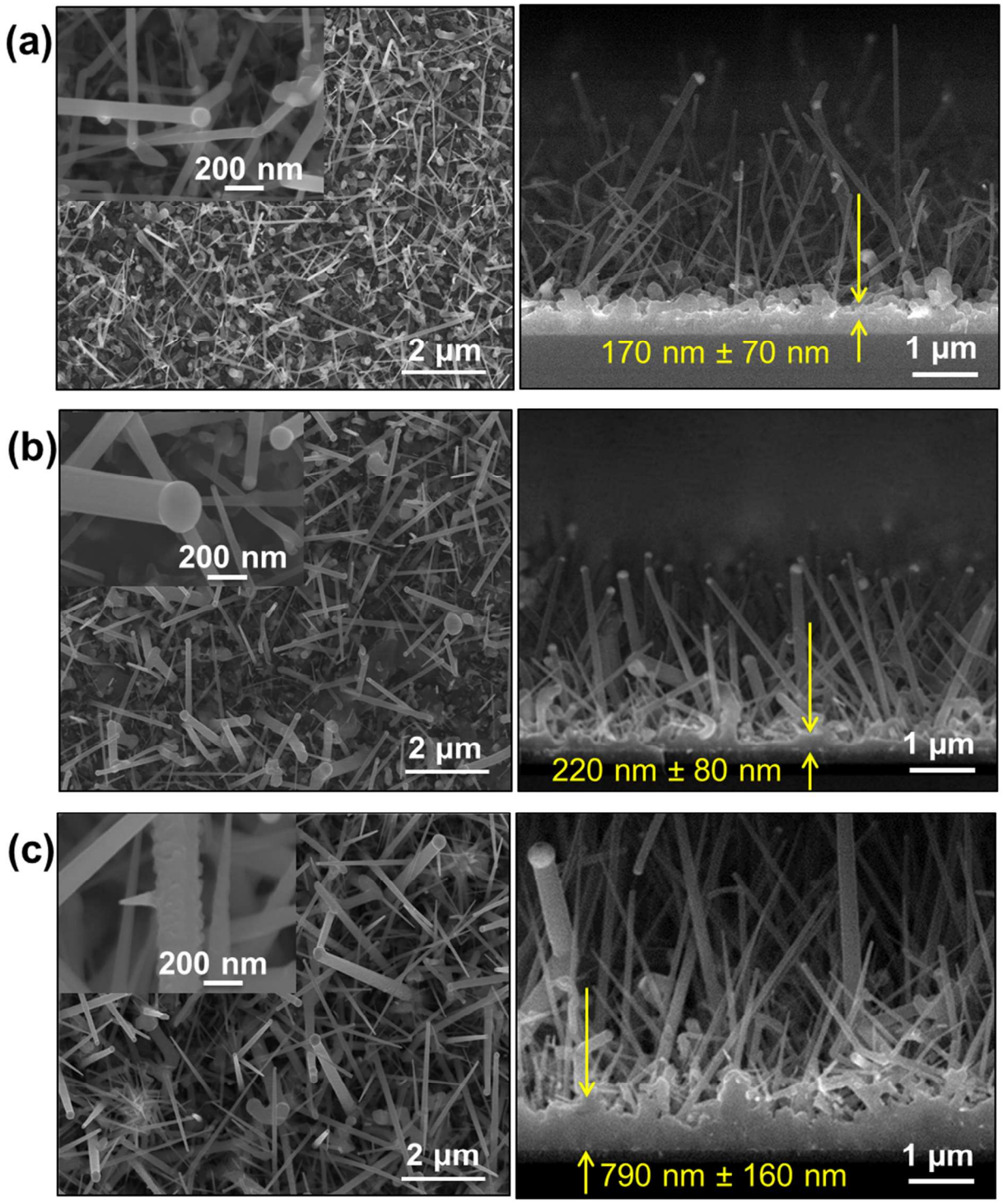

Figure 1: Plan-view (left-column) and cross-sectional (right column) SEM images of as synthesized nanowires. (a) 0.12mg-(320/2min); (b) 0.2mg-(360/2min); (c) 0.52mg-(360/5min); The images for samples grown with the remaining three sets of conditions are shown in the supplemental, Figure S1. Parasitic Ge films, formed at the nanowire base during VLS growth, are indicated by arrows in cross-sectional images.

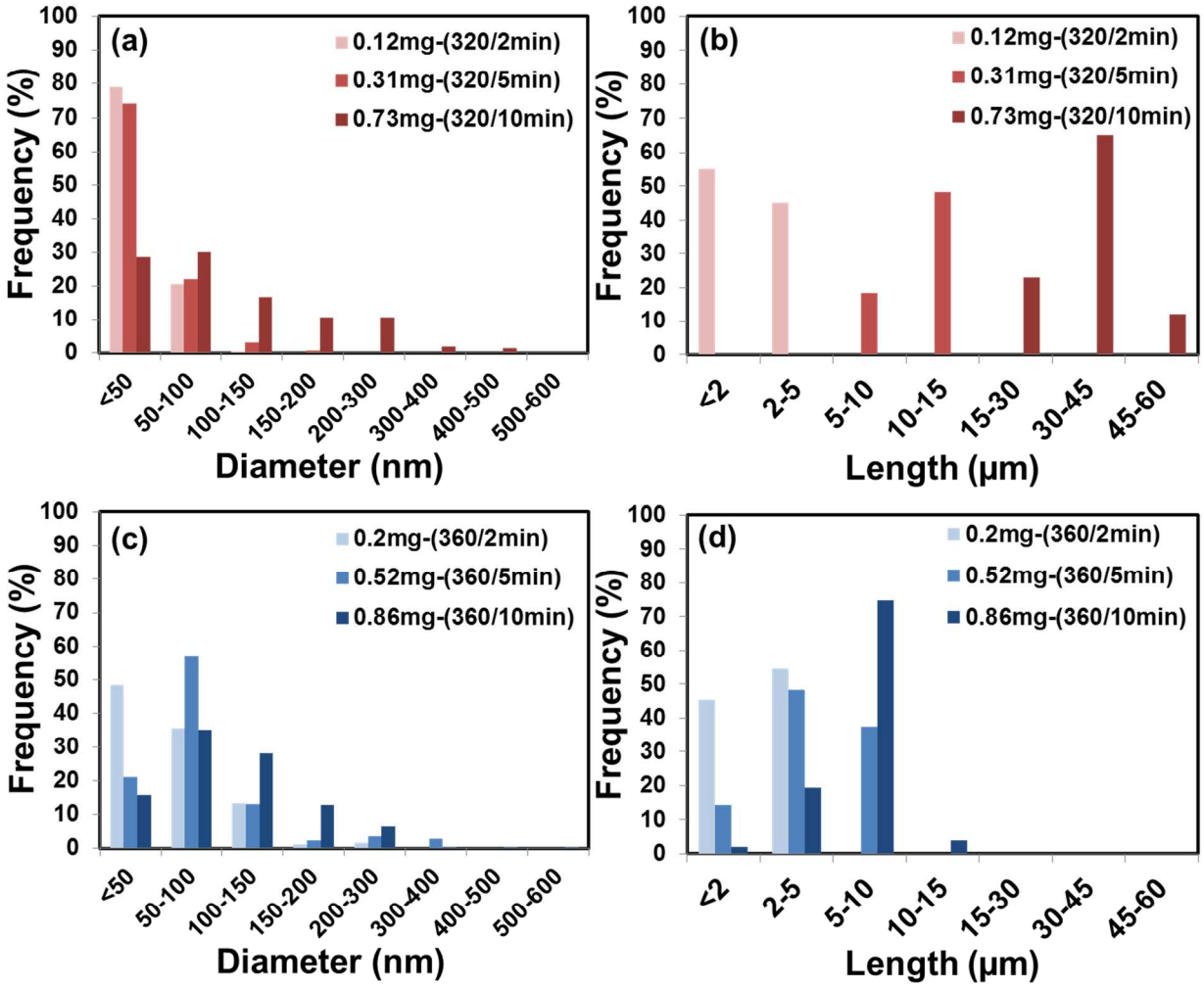

Figure 2: (a) – (d) Diameter and length distribution histograms of the as-synthesized GeNWs, grown at 320 °C and 360 °C.

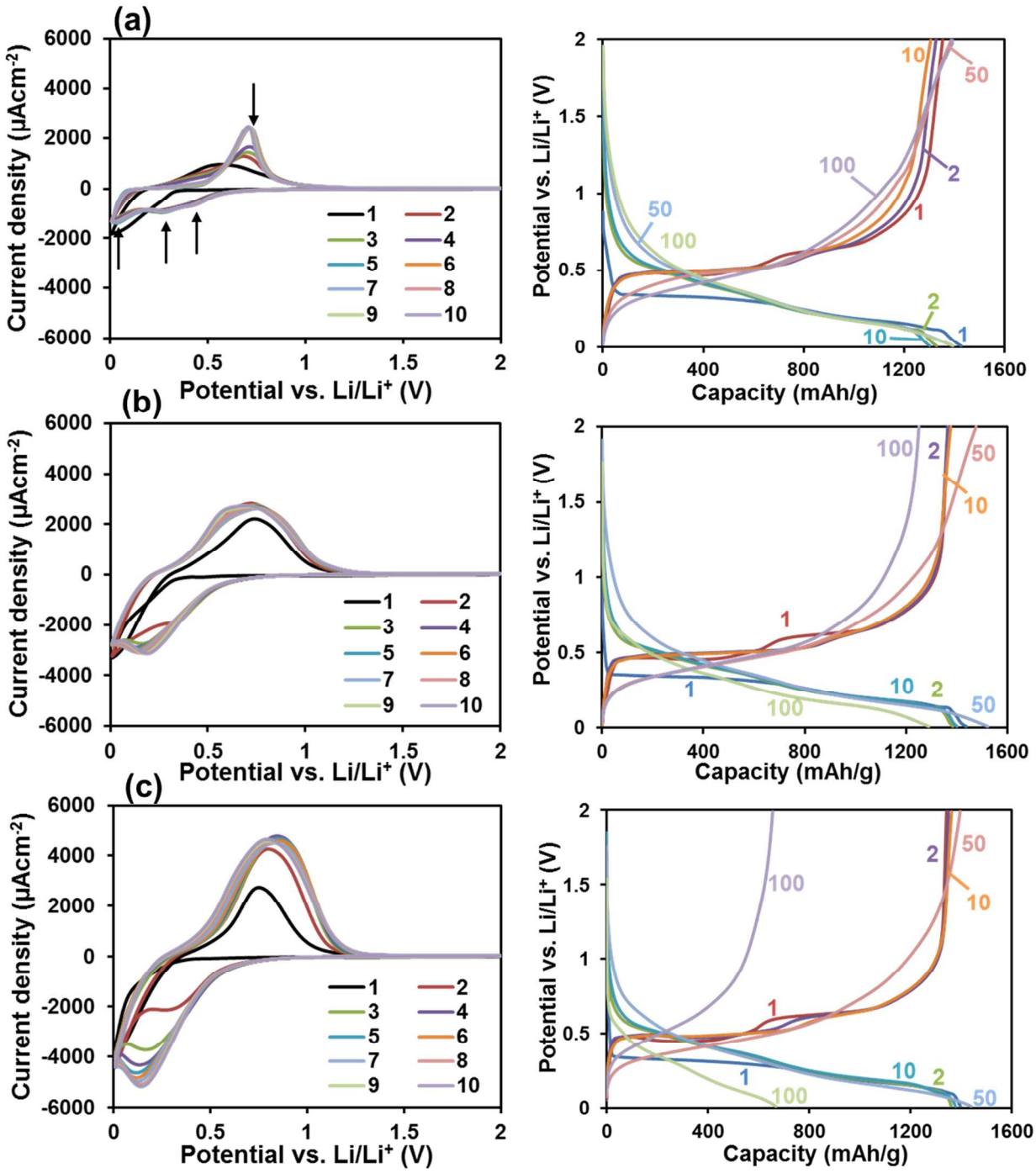

Figure 3: Cyclic voltammetry curves (left column) and constant-current voltage profiles (right column) of (a) 0.12mg-(320/2min), (b) 0.31mg-(320/5min), (c) 0.73mg-(320/10min), (d) 0.2mg-(360/2min), (e) 0.52-(360/5min), (f) 0.86-(360/10min) between 0 and 2V vs. Li/Li+ and 0.1C rate.

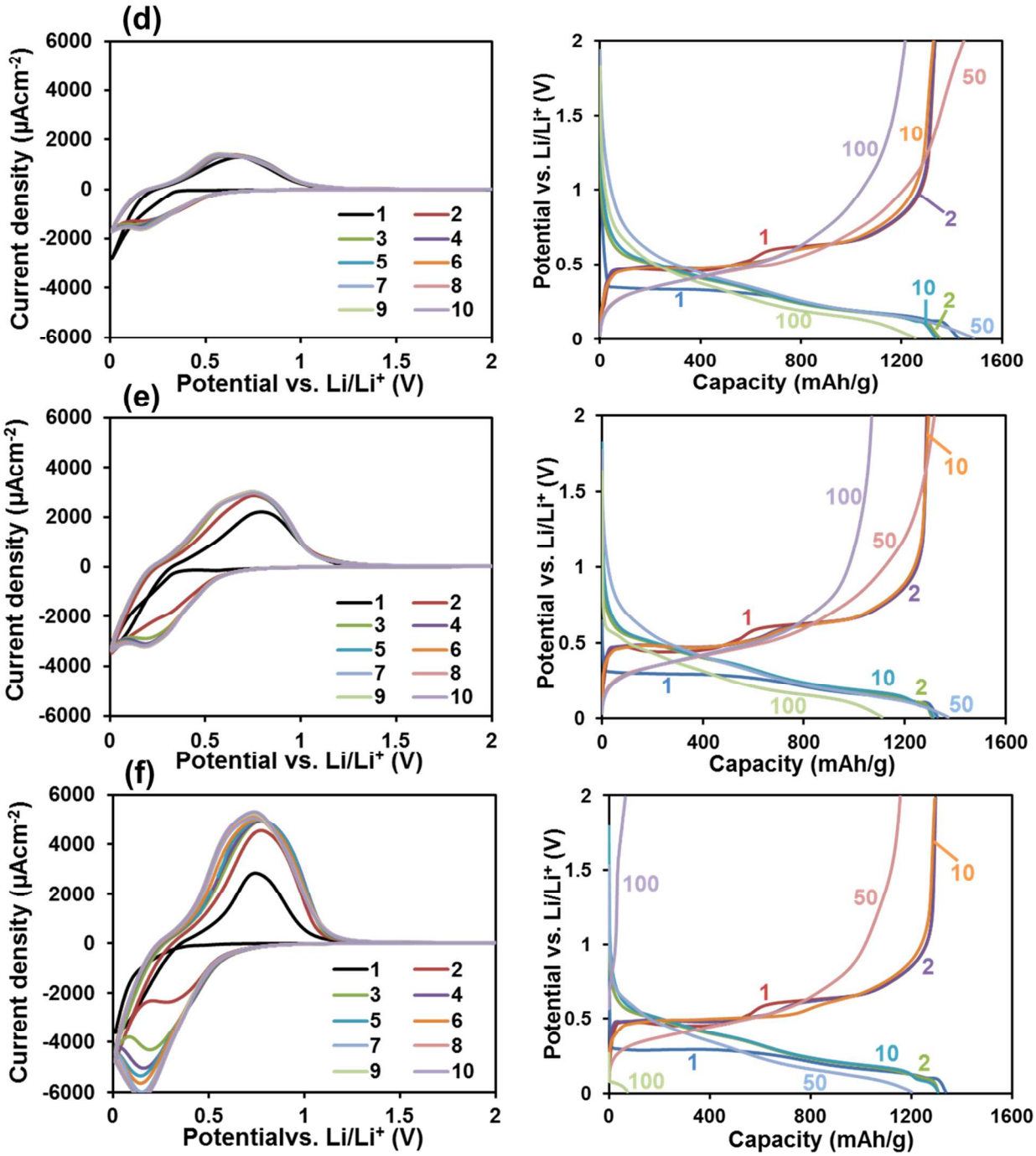

Figure 3, cont.: Cyclic voltammetry curves (left column) and constant-current voltage profiles (right column) of (d) 0.2mg-(360/2min), (e) 0.52-(360/5min), (f) 0.86-(360/10min) between 0 and 2V vs. Li/Li$^+$ and 0.1C rate.

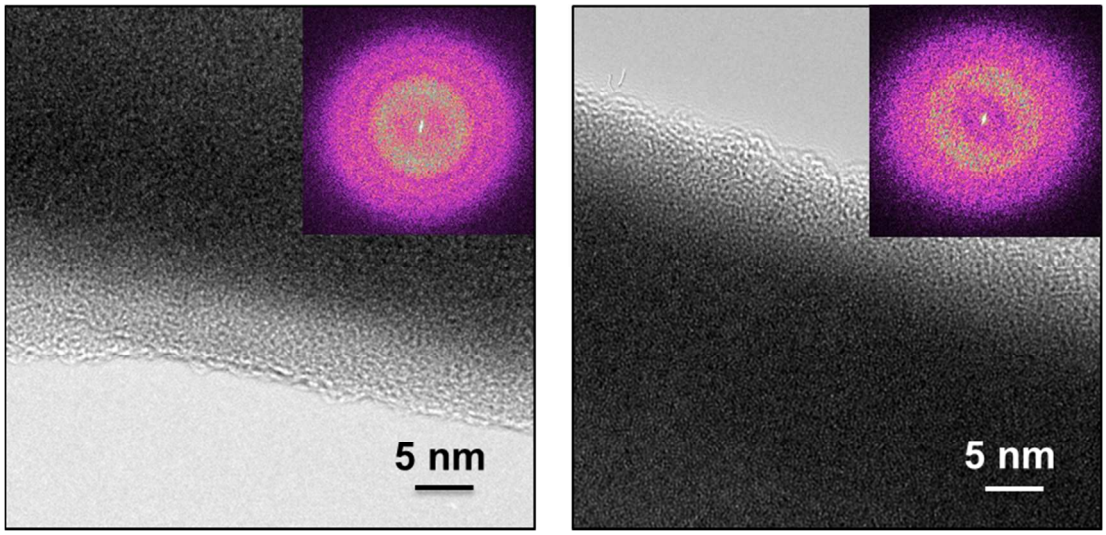

Figure 4: HRTEM and corresponding FFT images of representative sections of the 0.12mg-(320°C/2min) samples, after the first delithiation at 138 mA g^{-1}.

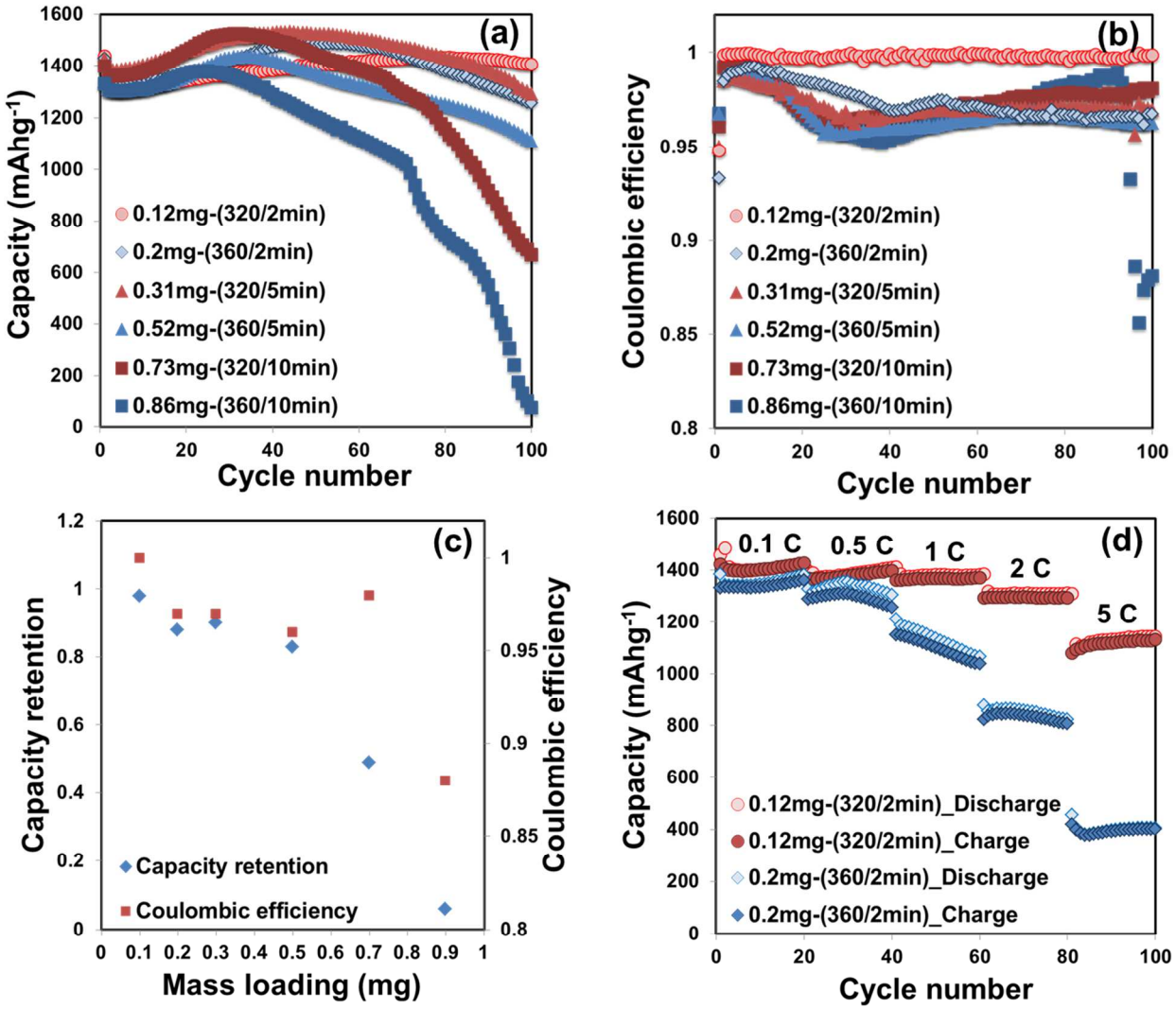

Figure 5: (a) Reversible capacity and (b) Coulombic efficiency (CE) versus cycle number, tested at 138 mA g^{-1}. (c) Cumulative comparison of capacity retention (at 100 cycles) and CE (at 50 cycles) versus mass loading. (d) Rate capability comparison of the 0.12 mg versus the 0.2 mg mass loading electrodes.

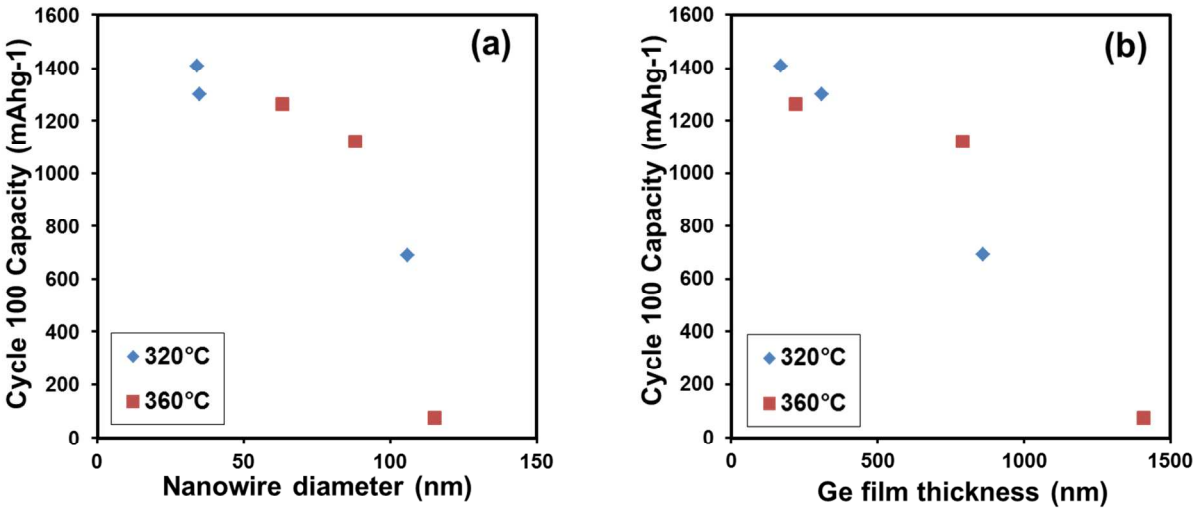

Figure 6: Cycle 100 capacity retention as a function of (a) the mean nanowire diameter, and (b) Ge parasitic film thickness.

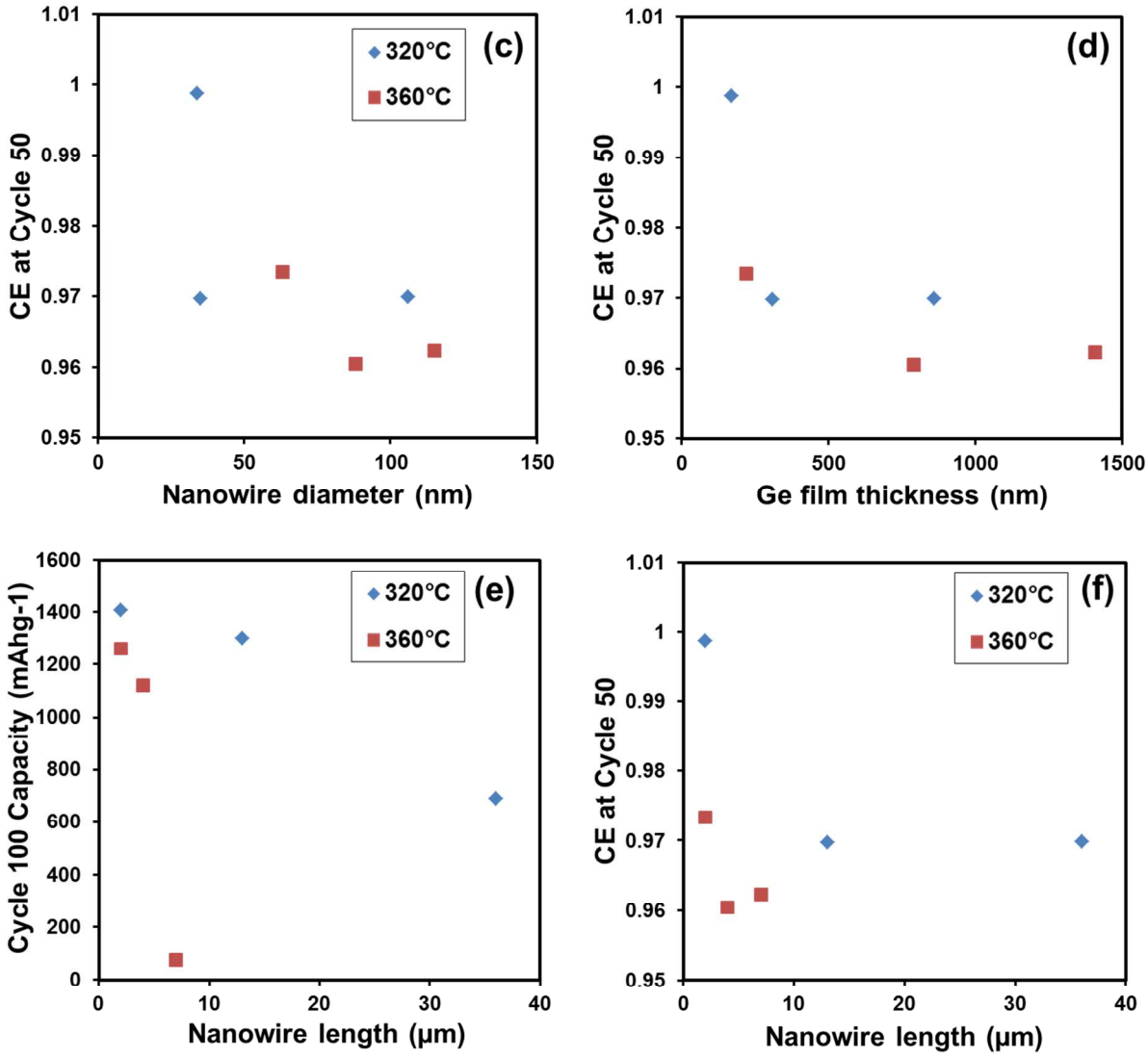

Figure 6, cont.: (c) – (d) CE (cycle 50) as a function of the mean nanowire diameter and parasitic Ge film thickness, (e) – (f) Cycling capacity retention (cycle 100) and CE (cycle 50) as a function of mean nanowire length.

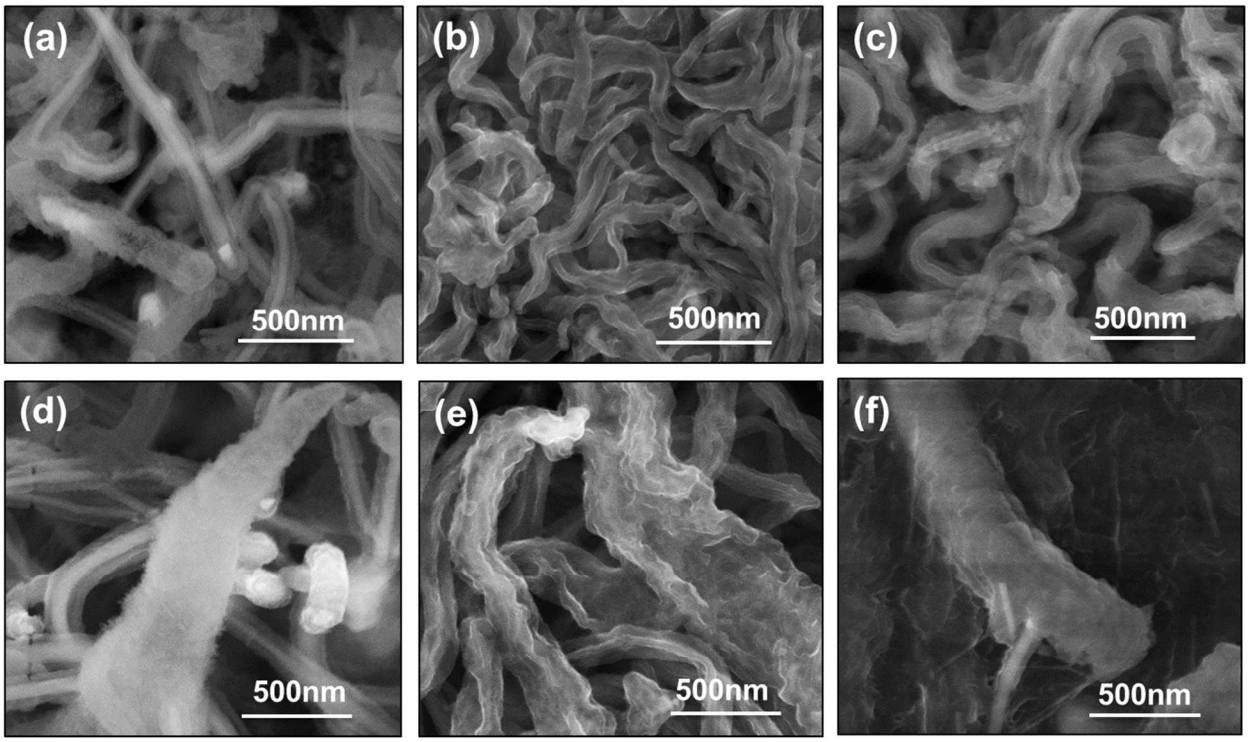

Figure 7: Plan-view SEM images of the cycled 0.12mg-(320/2min) for (a) 1 cycle, (b) 10 cycles, and (c) 100 cycles. Cycled 0.2mg-(360/2min) for (d) 1 cycle, (e) 10 cycles, and (f) 100 cycles.

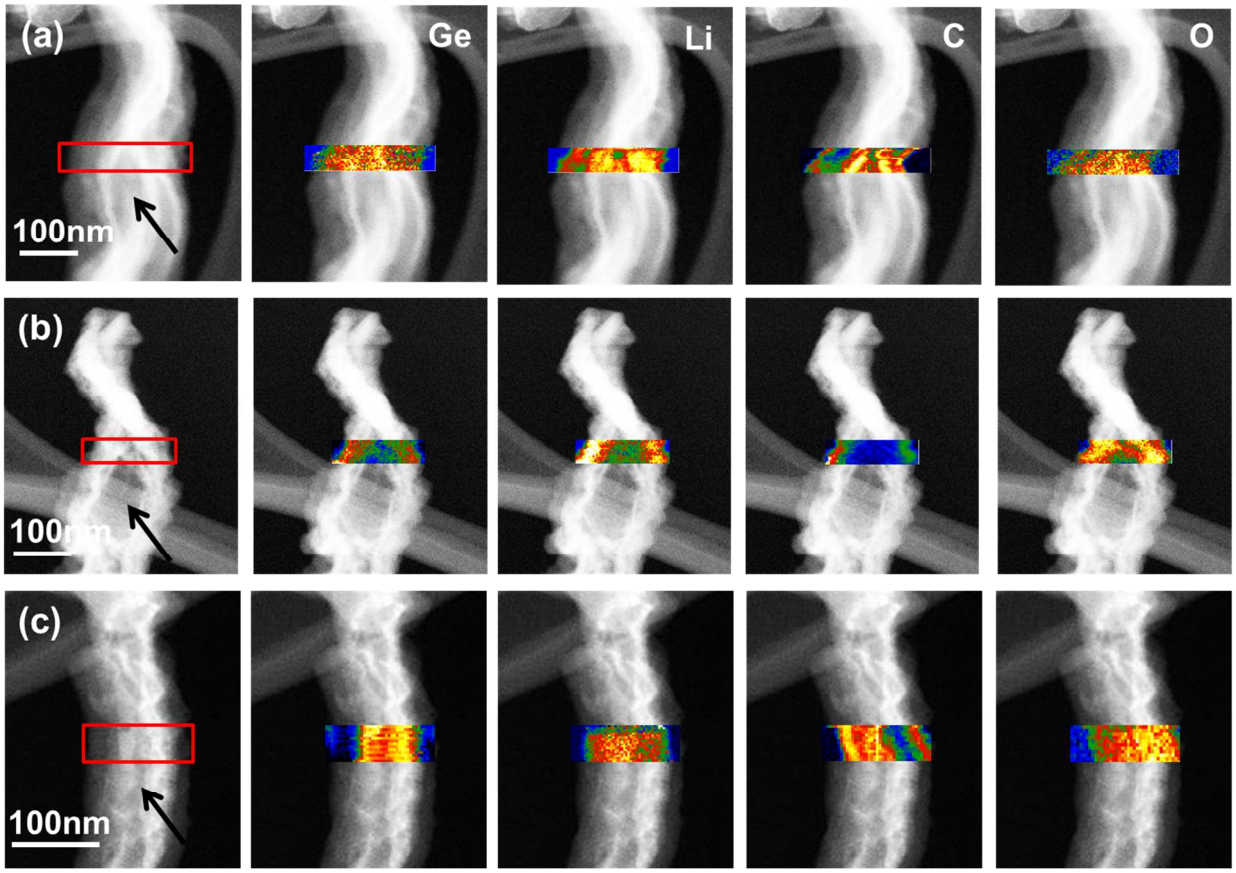

Figure 8: HAADF images and overlaid EELS maps of Ge, Li, C, and O for the post-100 cycles non-agglomerated nanowires located near the top surface of the electrode. (a) 0.12mg-(320/2min), (b) 0.73mg-(320/10min), and (c) 0.2mg-(360/2min). Arrows indicate the porosity near the center of the nanowires, which is running lengthwise.

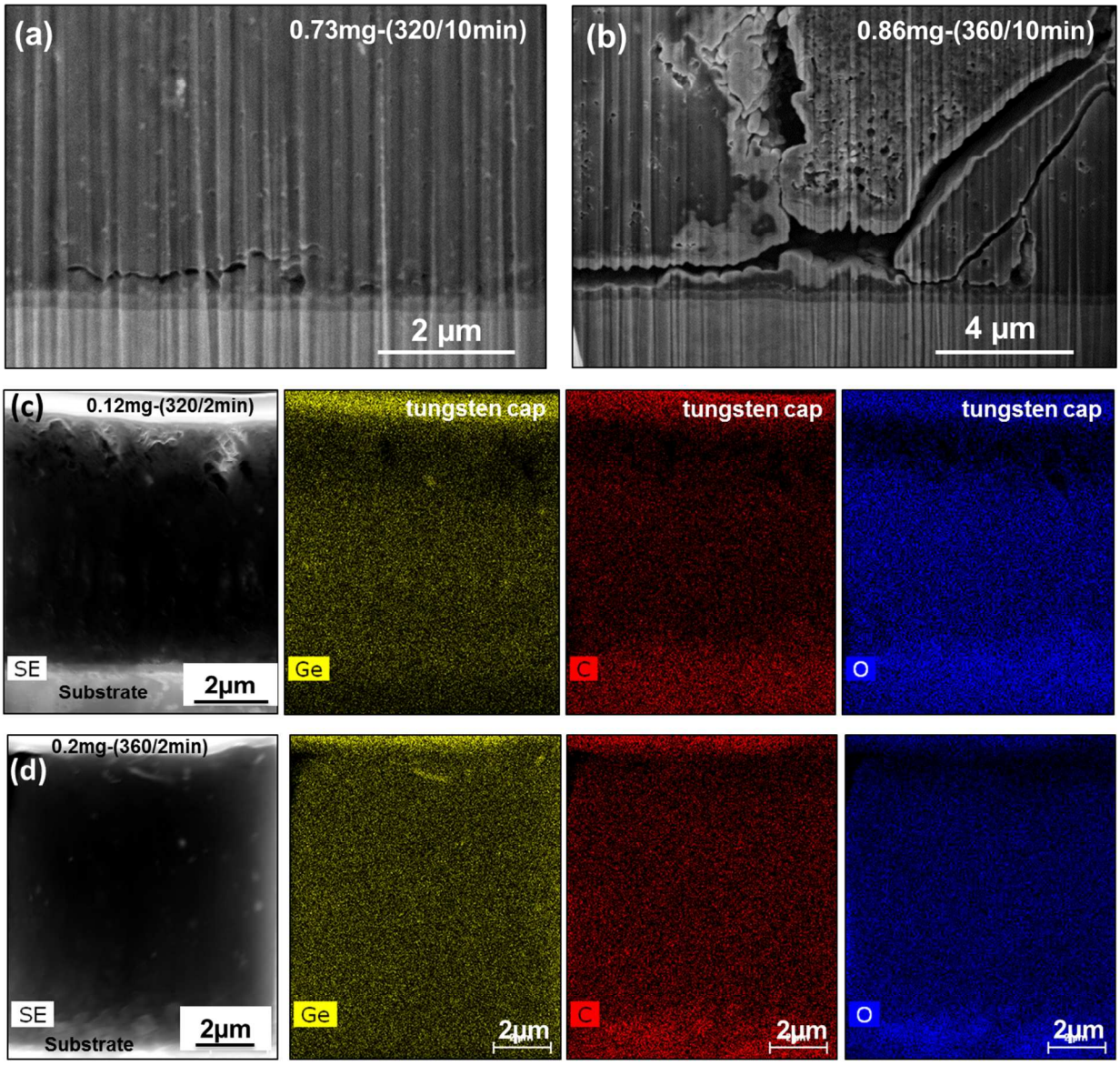

Figure 9: (a) and (b) FIB cross-sectional SEM images of the post-100 cycles 0.73mg-(320/10min) and 0.86mg-(360/10min) electrodes highlighting cracking at the current collector interface. (c) and (d) FIB cross-sectional images and elemental maps of germanium, carbon, and oxygen in the post-100 cycles 0.12mg-(320/2min) and 0.2mg-(360/2min) electrodes, highlighting enhanced SEI formation near the nanowire – current collector interface.

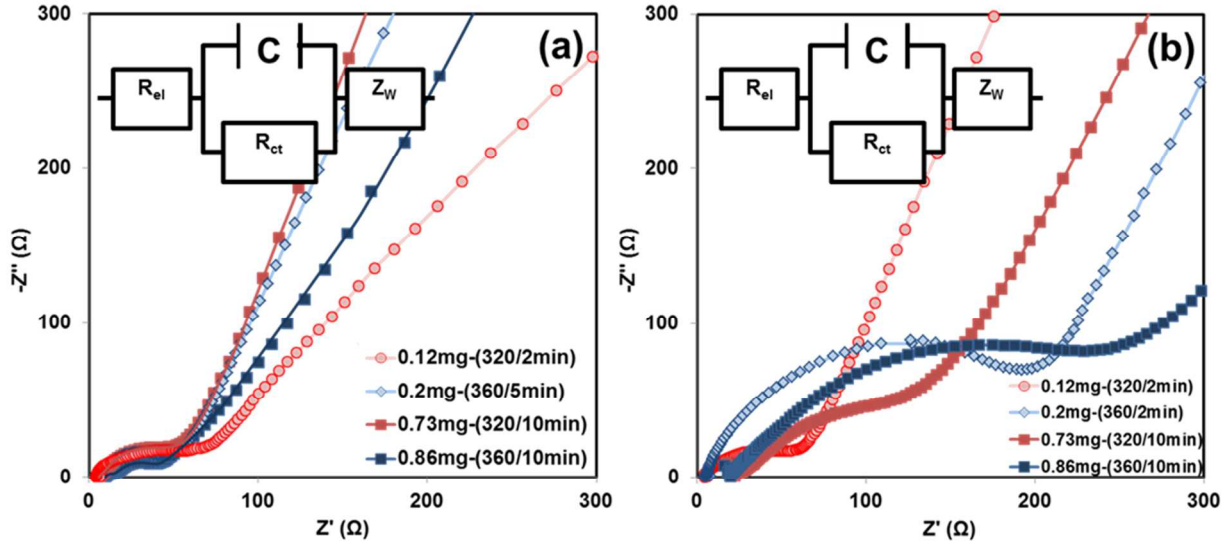

Figure 10: Electrochemical impedance (EIS) spectra of the GeNW electrodes after (a) 10 cycles, and (b) 100 cycles based on the equivalent circuit of two-electrode cells shown in the insets.

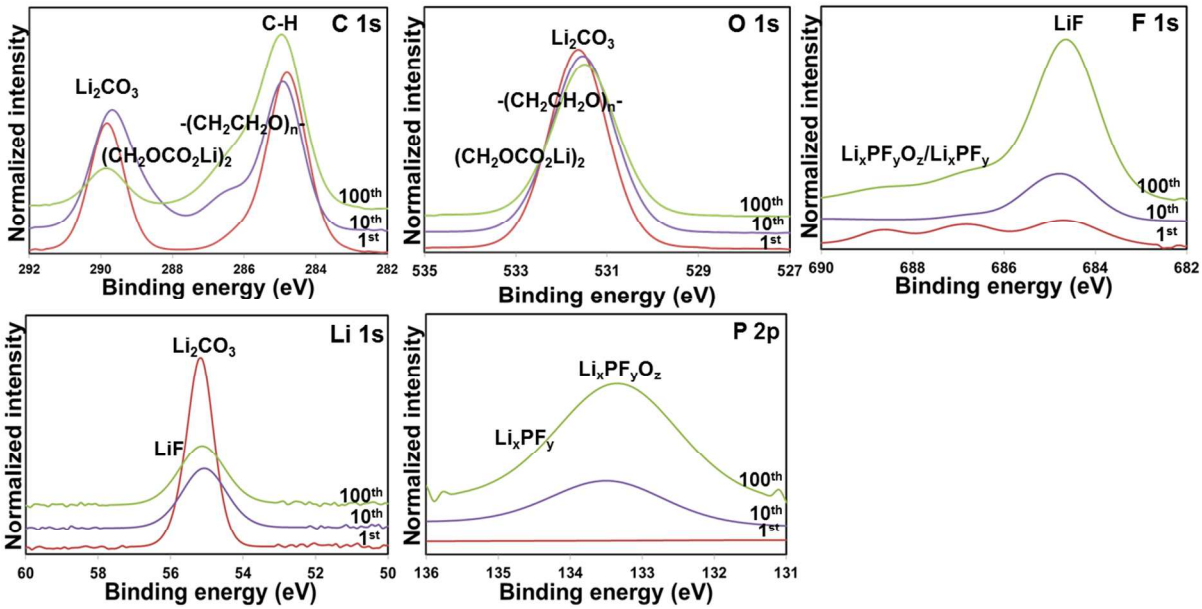

Figure 11: High resolution XPS spectra of 0.12mg-(320/2min) electrode after 1, 10 and 100 cycles.

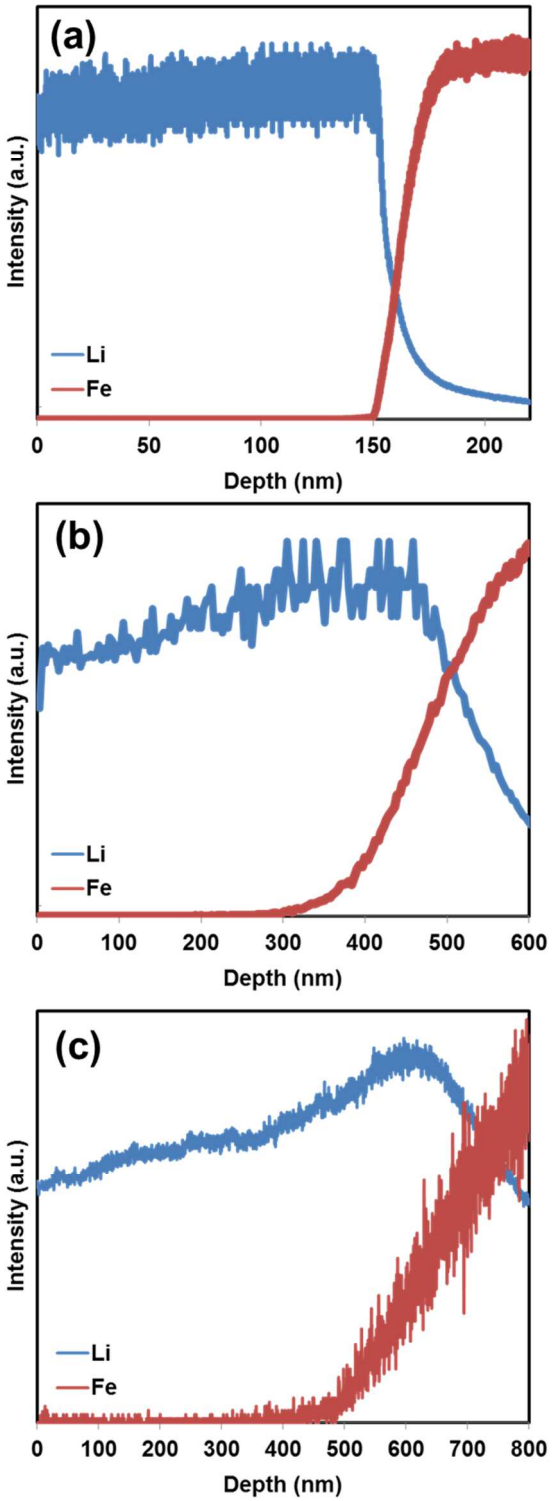

Figure 12: TOF-SIMS depth profiles of Li and Fe concentration through the thickness of lithiated Ge thin films on stainless steel substrate after the 2nd lithiation (a) – (c) 150, 300 and 500 nm Ge film thicknesses.

TOC: